AN ANALYSIS OF THE STELLAR MASS PROPERTIES OF DISTANT GALAXY CLUSTERS FROM THE MASSIVE AND DISTANT CLUSTERS OF WISE SURVEY (MADCOWS)

A Dissertation
IN
Physics and Astronomy
and
Electrical and Computer Engineering

Presented to the Faculty of the University
of Missouri—Kansas City in partial fulfillment of
the requirements for the degree

DOCTOR OF PHILOSOPHY

by
BANDON DECKER

BS Physics, Truman State University, Kirksville, MO, 2009

Kansas City, Missouri
2022

AN ANALYSIS OF THE STELLAR MASS PROPERTIES OF DISTANT GALAXY CLUSTERS FROM THE MASSIVE AND DISTANT CLUSTERS OF WISE SURVEY (MADCOWS)

Bandon Decker, Candidate for the Doctor of Philosophy Degree

University of Missouri–Kansas City, 2022

ABSTRACT

The epoch at redshift $z \sim 1$ and above is an important one for the study of the evolution of galaxy clusters, as this is the epoch where star formation in cluster cores in quenched. Most wide-area cluster surveys at this redshift range select clusters using the Sunyaev-Zel'dovich (SZ) effect, identifying clusters through their hot intracluster medium (ICM). In this work, I use the complementary Massive and Distant Clusters of WISE (MaDCoWS) infrared-selected survey to measure stellar mass properties of galaxy clusters at high redshift. I present initial measurements of the stellar mass fractions ($f_\star$) for a sample of MaDCoWS clusters and compare them to the stellar mass fractions of SZ-selected clusters in a similar mass and redshift range from the South Pole Telescope (SPT)-SZ Survey. I do not find a significant difference in mean $f_\star$ between the two selection methods, though we do find an unexpectedly large range in $f_\star$ for the SZ-selected clusters. I also make shallow

measurements of the composite $m_{3.6}$ luminosity function (LF) for the MaDCoWS clusters and find similar results to other studies of clusters at or near our redshift range. Adding optical and deeper mid-infrared data, I also present more complete stellar mass measurements and deeper luminosity functions for a sample of MaDCoWS clusters. Using SED-fitting of deep optical and mid-infrared photometry, I establish the membership of objects along the lines-of-sight to these clusters and calculate the stellar masses of member galaxies. The results follow a similar pattern of stellar mass fraction to the initial results, but higher values overall, and improved stellar mass errors. The LFs are even more improved, with the deeper data allowing me to fit both the characteristic magnitude and faint-end slope simultaneously. I found an evolution in these parameters consistent with passive evolution, but with more data needed to reduce the uncertainty.

APPROVAL PAGE

The faculty listed below, appointed by the Dean of the School of Graduate Studies, have examined a dissertation titled "An Analysis of the Stellar Mass Properties of Distant Galaxy Clusters from the Massive and Distant Clusters of WISE Survey (MaDCoWS)," presented by Bandon Decker, candidate for the Doctor of Philosophy degree, and hereby certify that in their opinion it is worthy of acceptance.

Supervisory Committee

Mark Brodwin, Ph.D., Committee Chair
Department of Physics & Astronomy

Daniel H. McIntosh, Ph.D.
Department of Physics & Astronomy

Paul Rulis, Ph.D.
Department of Physics & Astronomy

Masud Chowdhury, Ph.D., Inter-disciplinary Committee Chair
Department of Computer Science & Electrical Engineering

Deep Medhi, Ph.D.
Department of Computer Science & Electrical Engineering

CONTENTS

ILLUSTRATIONS

TABLES

ACKNOWLEDGEMENTS

I would like to thank my advisor, Dr Mark Brodwin, for all his support, teaching and encouragement over the many years of my graduate studies. Whilst it goes without saying that I could not have done this without him, it bears emphasising the positive role he has played in my development as a researcher.

I would also like to thank my parents, for supporting and encouraging my dream to become a scientist, even when it seemed very unlikely. And I want to thank my significant other, Rachel, for their love and support over the last year and more. They have made an extremely difficult time so much easier to bear.

Lastly, I would like to thank all of my collaborators with MaDCoWS and my colleagues in the UMKC Galaxy Evolution Group. I have learnt so much from the many telecons, meetings, and just conversations I have had with them over the years.

Thanks are also due to the UMKC School of Graduate Studies, whose arbitrary and pointless style requirements for this document have caused considerable frustration, delay and stress, which I really didn't have enough of otherwise. Thank you so, *so* much.

For Chapter 2: Support for CARMA construction was derived from the Gordon and Betty Moore Foundation, the Kenneth T. and Eileen L. Norris Foundation, the James S. McDonnell Foundation, the Associates of the California Institute of

Technology, the University of Chicago, the states of California, Illinois, and Maryland, and the National Science Foundation. CARMA development and operations are supported by the National Science Foundation under a cooperative agreement, and by the CARMA partner universities; the work at Chicago was supported by NSF grant AST- 1140019. Additional support was provided by PHY- 0114422. This work is based in part on observations made with the *Spitzer Space Telescope*, which is operated by the Jet Propulsion Laboratory, California Institute of Technology under a contract with NASA. Support for this work was provided by NASA through an award issued by JPL/Caltech. This publication makes use of data products from the *Wide-field Infrared Survey Explorer*, which is a joint project of the University of California, Los Angeles, and the Jet Propulsion Laboratory/California Institute of Technology, funded by the National Aeronautics and Space Administration. Some of the data presented herein were obtained at the W.M. Keck Observatory, which is operated as a scientific partnership among the California Institute of Technology, the University of California and the National Aeronautics and Space Administration. The Observatory was made possible by the generous financial support of the W.M. Keck Foundation. This work was based in part on observations obtained at the Gemini Observatory, which is operated by the Association of Universities for Research in Astronomy, Inc., under a cooperative agreement with the NSF on behalf of the Gemini partnership: the National Science Foundation (United States), the National Research Council (Canada), CONICYT (Chile), Ministerio de Ciencia, Tecnología e Innovación Productiva (Argentina), and Ministério da Ciência,

Tecnologia e Inovação (Brazil). This work has made use of data from the European Space Agency (ESA) mission *Gaia* (`https://www.cosmos.esa.int/gaia`), processed by the *Gaia* Data Processing and Analysis Consortium (DPAC, `https://www.cosmos.esa.int/web/gaia/dpac/consortium`). Funding for the DPAC has been provided by national institutions, in particular the institutions participating in the *Gaia* Multilateral Agreement. Funding for this program is provided by NASA through the NASA Astrophysical Data Analysis Program, award NNX12AE15GB. Support for this work was provided by the National Aeronautics and Space Administration through Chandra Award Number GO6-17130X issued by the Chandra X-ray Center, which is operated by the Smithsonian Astrophysical Observatory for and on behalf of the National Aeronautics Space Administration under contract NAS8-03060.

For Chapter 3: The work of T.C., P.E., and D.S. was carried out at the Jet Propulsion Laboratory, California Institute of Technology, under a contract with NASA. F.R. acknowledges financial supports provided by NASA through SAO Award Number SV2- 82023 issued by the Chandra X-Ray Observatory Center, which is operated by the Smithsonian Astrophysical Observatory for and on behalf of NASA under contract NAS8-03060. This work is based in part on observations made with the *Spitzer Space Telescope*, which is operated by the Jet Propulsion Laboratory, California Institute of Technology under a contract with NASA. Support for this work was provided by NASA through an award issued by JPL/Caltech. This publication makes use of data products from the *Wide-field Infrared Survey*

Explorer, which is a joint project of the University of California, Los Angeles, and the Jet Propulsion Laboratory/California Institute of Technology, funded by the National Aeronautics and Space Administration. This work was based in part on observations obtained at the Gemini Observatory, which is operated by the Association of Universities for Research in Astronomy, Inc., under a cooperative agreement with the NSF on behalf of the Gemini partnership: the National Science Foundation (United States), the National Research Council (Canada), CONICYT (Chile), Ministerio de Ciencia, Tecnología e Innovación Productiva (Argentina), and Ministério da Ciência, Tecnologia e Inovação (Brazil). Funding for this program is provided by NASA through the NASA Astrophysical Data Analysis Program, award 80NSSC19K0582. Support for this work was provided by the National Aeronautics and Space Administration through Chandra Award Number GO7-18123A issued by the Chandra X-ray Center, which is operated by the Smithsonian Astrophysical Observatory for and on behalf of the National Aeronautics Space Administration under contract NAS8-03060. Based on observations with the NASA/ESA Hubble Space Telescope obtained at the Space Telescope Science Institute, which is operated by the Association of Universities for Research in Astronomy, Incorporated, under NASA contract NAS5-26555. Support for program number HST-GO-14456 was provided through a grant from the STScI under NASA contract NAS5-26555.

CHAPTER 1

INTRODUCTION

Sing, o Muse, of the stellar mass properties of high-redshift, infrared-selected galaxy clusters!

Galaxy clusters are the result of hierarchical growth from primordial overdensities in the universe. Despite the name, galaxies only form a small part of the overall mass of galaxy clusters. Most of the mass is a huge halo of dark matter that forms a massive gravitational potential well. In this well is a hot gas of charged particles, known as the intracluster medium (ICM) as well as the galaxies themselves which are primarily made of stars. Because they have collapsed down from such a large fraction of the early universe, they are expected to contain a fair sampling of the ratio of dark matter to baryonic matter (non-dark matter, in this case the stars and gas) seen in the universe as a whole (e.g., White et al., 1993). Studies of clusters at low redshift—that is, in the nearby universe—such as Gonzalez et al. (2013), have found baryon fractions—the fraction of baryonic matter relative to all matter—comparable to what is expected for the universe as a whole, approximately 15%. Whilst the baryon fraction in clusters is comparable to the expected value, there is more variation in how the baryons are distributed between the two states in which we see baryons in clusters: stars in galaxies and the hot ICM. This variance in the partitioning of baryons between gas (the gas mass fraction, $f_{\rm gas}$) and stars (the

stellar mass fraction, $f_\star$) can give us insight into the physical processes in the cluster that convert baryonic matter from gas to stars. For that reason, we want to look at how these mass fractions in clusters are related to other cluster properties, such as mass and redshift. Gonzalez et al. (2013) found a decreasing trend of stellar mass fraction with total cluster mass—suggesting that lower mass clusters were better able to form stars—and a corresponding increase in gas mass fraction, making for a constant total baryon fraction.

Galaxy clusters in the local universe, such as those studied by Gonzalez et al. (2013) generally do not have any star formation in their cores. By looking at higher redshift, at more distant clusters, we can study them as they were earlier in the history of the universe. Brodwin et al. (2013) showed that the trend seen at low redshift reverses at high redshift, and around $z \sim 1.4$—about nine billion years ago—galaxies in the cores of clusters form stars at an even higher rate than galaxies in the outside of clusters—known as field galaxies. This is the opposite of what is seen at low redshifts, where field galaxies have higher star formation rates than galaxies in the cores of clusters. Something happens to clusters at $z \sim 1$ to quench this star formation and turn clusters into the 'red and dead' giants we see in the local universe.

To try to understand the mechanism by which star formation is quenched in these clusters, I want to measure the stellar mass fractions of clusters at this epoch, as well as a related property, the luminosity function (LF). The cluster LF is a measure of the number density of cluster galaxies as a function of the apparent

brightness of the galaxies in a certain wavelength band, measured in magnitudes. Magnitudes are a logarithmic scale in which a value five magnitudes larger is 100 times fainter. Cluster LFs are described by a Schechter function (Schechter, 1976), in which there are very few galaxies at the brightest end of the distribution, but the number density rises steeply going toward fainter magnitudes, until it hits a so-called characteristic magnitude, after which the number densities follow a roughly flat power law. Measuring the LF in the rest-frame near infrared (NIR)—around a wavelength of 1.6μm—tells us about the history of how galaxies have assembled their stellar mass, as this light is light emitted from the old stars that make up the bulk of a galaxy's stellar mass. The specific parameters of the NIR cluster LF are a product of the stellar mass assembly history of the cluster.

However, studying the stellar mass fractions and luminosity functions of clusters at this redshift range is complicated by the difficulty of detecting clusters at this distance. Most of the cluster surveys at $z \sim 1$ and above detect clusters by looking for the cluster ICM, using the Sunyaev-Zel'dovich (SZ) effect (Sunyaev & Zeldovich, 1972, 1980). The SZ effect is a distortion of the cosmic microwave background (CMB) radiation—relic light from the early universe—that is scattered to higher energies as it passes through the cluster ICM. It is an efficient method of detecting distant clusters, as this effect does not diminish with redshift. But using a sample of clusters detected only on one property—in this case the ICM—can potentially bias the measurement of that property. In addition, measuring the properties of the LF requires deep enough mid-IR data to jointly fit both the characteristic

magnitude and faint-end slope of the Schechter function, which is very costly.

Nor do hydrodyamic simulations of large-scale structures shed much light on the issues of selection bias and luminosity functions. The range of scales between where the feedback processes that affect the partitioning of baryons take place, and the dark matter haloes and sub-haloes is so large as to be a huge challenge for even the most modern computations. The BAHAMAS project (McCarthy et al., 2017) explicitly attempts to do both. But in addition to mostly producing clusters and groups with lower halo masses than MaDCoWS clusters, it also cannot resolve galaxies with a stellar mass less than 10^{10} $M_{\odot}$. By contrast, the follow-up observations of MaDCoWS clusters are sensitive to galaxies with stellar masses below 10^{8} $M_{\odot}$. Other studies such as IllustrisTNG (Pillepich et al., 2017) fail to reproduce the ranges of stellar mass fractions we see in clusters.

To study this problem of measurement bias, I have used galaxy clusters taken from the Massive and Distant Clusters of WISE Survey (MaDCoWS Gonzalez et al., 2019). MaDCoWS used all-sky data from the Wide-field Infrared Survey Explorer (*WISE*) and ground-based optical data to identify clusters at $z \geq 1$ across the whole extragalactic sky. This offers both a complementary selection to SZ-based surveys, in that MaDCoWS selects on stellar mass rather than the ICM, and a much larger survey area, allowing MaDCoWS to find the rarest clusters at this redshift range. MaDCoWS also has very deep mid-IR data on a number of clusters, allowing me to robustly measure the LF.

This thesis aims to study if there is a bias in the cluster properties arising

from how cluster samples are selected and to shed light on the stellar mass properties of galaxies at or near the transition redshift where star formation shuts off.

This thesis is laid out as follows. In Chapter 2, I measure the $f_\star$ in the same way for both MaDCoWS clusters and for SZ-selected clusters from the South Pole Telescope (SPT) and directly compare them to test if the differing selection methods produce a meaningful difference in the measured properties of the clusters. In Chapter 3, I use deeper data to improve upon the measurement of $f_\star$ for MaDCoWS clusters and I also use it to measure composite LFs for both the full sample, and the sample split into two bins of redshift. In Chapter 4 I present my conclusions. Throughout this thesis, I use a concordance ΛCDM cosmology of $\Omega_m = 0.3$, $\Omega_\Lambda = 0.7$ and $H_0 = 70$ km s^{-1}Mpc^{-1} and I express all magnitudes in the AB system. Cluster masses and radii are given in terms of M_{500} and r_{500}, where the latter is the radius inside which the cluster density is 500 times the critical density of the universe and the former is the mass inside that radius.

CHAPTER 2

THE MASSIVE AND DISTANT CLUSTERS OF WISE SURVEY VI: STELLAR MASS FRACTIONS OF A SAMPLE OF HIGH-REDSHIFT INFRARED-SELECTED CLUSTERS

Published in *Decker et al., 2019, ApJ, 878, 72*

DOI: 10.3847/1538-4357/ab12d7

Abstract

We present measurements of the stellar mass fractions ($f_\star$) for a sample of high-redshift ($0.93 \leq z \leq 1.32$) infrared-selected galaxy clusters from the Massive and Distant Clusters of WISE Survey (MaDCoWS) and compare them to the stellar mass fractions of Sunyaev-Zel'dovich (SZ) effect-selected clusters in a similar mass and redshift range from the South Pole Telescope (SPT)-SZ Survey. We do not find a significant difference in mean $f_\star$ between the two selection methods, though we do find an unexpectedly large range in $f_\star$ for the SZ-selected clusters. In addition, we measure the luminosity function of the MaDCoWS clusters and find $m^* = 19.41 \pm 0.07$, similar to other studies of clusters at or near our redshift range. Finally, we present SZ detections and masses for seven MaDCoWS clusters and new spectroscopic redshifts for five MaDCoWS clusters. One of these new clusters, MOO J1521+0452 at $z = 1.31$, is the most distant MaDCoWS cluster confirmed to date.

2.1 Introduction

Galaxy clusters are the largest gravitationally-bound objects in the universe and a thorough knowledge of their composition, history and evolution is important for both cosmological abundance analyses and galaxy formation/evolution studies in the richest environments (e.g., Allen et al., 2011; Kravtsov & Borgani, 2012). It has been found in simulations (e.g., Ettori et al., 2006; Conroy et al., 2007) and suggested observationally (e.g., Lin et al., 2003) that the fraction of a cluster's total mass that is in stars, $f_\star$, is related to the star formation history of that cluster. It follows that measuring $f_\star$ and $f_{\rm gas}$, the fraction of mass in the intracluster medium (ICM), in clusters covering a range of masses and ages can constrain the growth and evolutionary history of clusters and the galaxies therein. A proper account of the total stellar mass of a cluster is also a necessary component of calculating the total baryon fraction in a cluster. The cluster baryon fraction is expected to be close to the total baryon fraction of the universe (White et al., 1993), but previous studies (e.g., Gonzalez et al., 2007, 2013; Lin et al., 2012) have found somewhat lower fractions. The size of this discrepancy and its relation to the total mass of the cluster is important cosmologically and can also provide clues to the baryon physics in clusters (He et al., 2005). Coupled with studies that show a cessation of star formation in the cores of large clusters since high redshifts (e.g., Brodwin et al., 2013), such measurements can shed light on the feedback processes involved in the partition of baryons into stars and gas in clusters.

Several studies have previously looked at the stellar mass fraction of clusters

and generally find a trend of decreasing $f_\star$ with increasing halo mass. However, with the exception of van der Burg et al. (2014), all these studies were at $z \leq 0.6$ (Lin et al., 2003; Gonzalez et al., 2007; Andreon, 2010; Zhang et al., 2011; Lin et al., 2012; Gonzalez et al., 2013) and/or used samples that selected clusters entirely on the strength of the signal from the ICM, either from X-ray observations or from the Sunyaev-Zel'dovich (SZ, Sunyaev & Zeldovich, 1970, 1972) decrement (Giodini et al., 2009; Hilton et al., 2013; Chiu et al., 2016, 2018). It is possible, for both SZ- and X-ray-selected samples, that selecting on an observable related to the ICM pressure or X-ray luminosity (approximately ICM density squared) could produce a sample with a bias toward a higher gas mass fraction, presumably at the expense of $f_\star$ (assuming a constant baryon fraction at fixed mass). Such a bias may also prevent the scatter in $f_{\rm gas}$ from being fairly measured, though the measured scatter in $f_\star$ should be less affected, as the cluster selection does not have any intrinsic bias toward or against stellar mass.

To explore these issues, we use high-redshift infrared-selected clusters from the Massive and Distant Clusters of *WISE* Survey (MaDCoWS, Gettings et al., 2012; Stanford et al., 2014; Brodwin et al., 2015; Gonzalez et al., 2015; Mo et al., 2018; Gonzalez et al., 2019). MaDCoWS uses the *Wide-field Infrared Survey Explorer* (*WISE*, Wright et al., 2010) All *WISE* data release (Cutri, 2013) and PanSTARRS (Chambers et al., 2016) optical data to identify overdensities of galaxies at $z \sim 1$ across nearly the entire extragalactic sky. It therefore can provide a greater mass range at high-redshift than SZ surveys because it simultaneously has the area to

find the rarest, most massive objects at high redshifts—such as MOO J1142+1527 ($M_{500} = 5.36 \times 10^{14}\ M_{\odot}$, $z = 1.19$) reported in Gonzalez et al. (2015) and MOO J1521+0452 ($M_{500} = 3.59 \times 10^{14}\ M_{\odot}$, $z = 1.31$) described herein—and the sensitivity to detect clusters to the same or lower mass limit of current SZ surveys.

In this work we use SZ observations and follow-up *Spitzer Space Telescope* data on twelve MaDCoWS clusters to calculate $f_\star$ for this high-redshift, infrared-selected sample. We also analyze a comparable sample of SZ-selected clusters from the South Pole Telescope (SPT)-SZ survey (Bleem et al., 2015) using the same methodology and compare these to the same quantities measured for our infrared-selected MaDCoWS clusters. Because the SPT sample is SZ-selected, it fairly measures the average value and scatter in $f_\star$.

The cluster samples and data we use are described in §3.2 and the analysis thereof is described in §3.3. We present the results of our $f_\star$ measurements in §3.4 and discuss them in §3.5. Our conclusions are in §3.6. Throughout we use AB magnitudes and a concordance ΛCDM cosmology of $\Omega_m = 0.3$, $\Omega_\Lambda = 0.7$ and $H_0 = 70$ km s^{-1}Mpc^{-1}. We define r_{500} as the radius inside which a cluster has an average density 500 times the critical density of the universe and M_{500} as the mass inside that radius.

2.2 Cluster Sample and Data

For our infrared-selected sample, we use twelve MaDCoWS clusters with halo masses calculated from SZ detections from the Combined Array for Research in Millimeter-wave Astronomy (CARMA). SZ observations of four of these (MOO J0319-0025, MOO J1014+0038, MOO J1155+3901 and MOO J1514+1346) are described in Brodwin et al. (2015). A fifth, MOO J1142+1527, the most massive cluster yet found by any method at $z \geq 1.15$, is reported in Gonzalez et al. (2015). Here we report new SZ detections for the other seven clusters, along with total masses and radii determined from those data as well as new masses and radii of the previously-reported clusters derived from an updated reduction of the CARMA data, described in §2.3.1. All twelve clusters have imaging with the Infrared Array Camera (IRAC, Fazio et al., 2004) on *Spitzer*, which enables us to determine the stellar mass of the clusters as described in §2.4.1.

The SZ-selected clusters we use for comparison are drawn from the SPT-SZ survey described in Bleem et al. (2015). To ensure we are making a fair comparison between the infrared- and SZ-selected samples, we only use the 33 SPT clusters that lie in a similar range of mass and redshift as the MaDCoWS clusters, specifically $0.9 < z < 1.35$ and $M_{500} < 1 \times 10^{15}\ M_{\odot}$, and for which comparable IRAC data exist. We do not impose a lower limit on the mass for the SPT subsample as the SPT-SZ catalog has a higher mass threshold than MaDCoWS at these redshifts. A plot of mass versus redshift for both samples is shown in Figure 1.

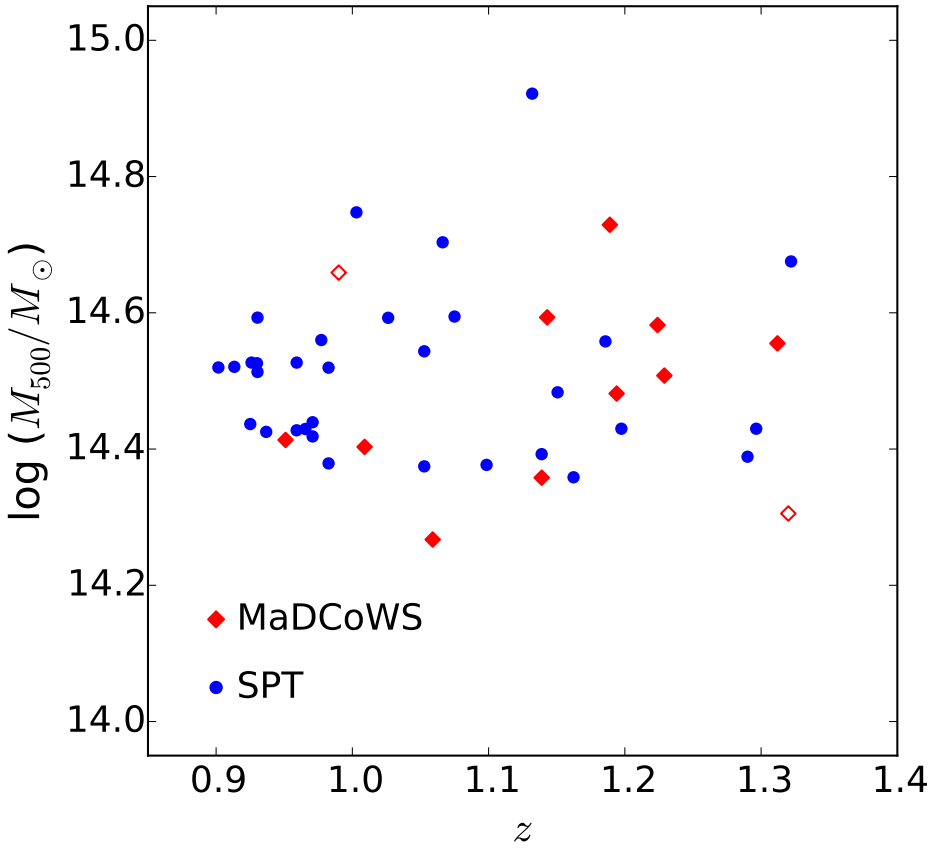

Figure 1 Plot showing the distribution of the MaDCoWS clusters (red diamonds) and the comparison SPT clusters (blue circles) in mass and redshift. The open diamonds denote the MaDCoWS clusters in this analysis that currently lack spectroscopic redshifts.

2.2.1 CARMA Data

Before its closure in early 2015, CARMA was a heterogenous 23-element interferometer with six 10.4 m antennae, nine 6.1 m antennae and eight 3.5 m antennae. All of the antennae were equipped with 30 and 90 GHz receivers and the 10.4 and 6.1 m antennae had additional 230 GHz receivers. CARMA had two correlators, a wide-band (WB) and spectral-line (SL) correlator, and the 3.5 m antennae could operate as an independent array (CARMA-8 mode) or alongside the other 15 antennae in CARMA-23 mode. In its most compact 'E' configuration, the shortest CARMA baselines provided an appropriate beam size for SZ observations while the longer baselines enabled point source identification and subtraction.

The CARMA data for the seven new clusters were taken in the summer and autumn of 2014 and the observation dates of all twelve of our MaDCoWS clusters, as well as the on-source observation times excluding observations of the gain and flux calibrators, are given in Table 1. Point source-subtracted SZ maps of the seven clusters newly reported here are shown in Figure 2. The maps are in units of signal-to-noise with negative signal to denote the SZ effect being a decrement at 30 GHz. A 4kλ taper was applied to the *uv* data to produce an illustrative beam size and the maps were CLEANed (Högbom, 1974) in a box $4'$ on a side and centered on the SZ centroid.

Table 1. Summary of CARMA observations and properties of MaDCoWS clusters

Cluster ID	RA (J2000)	Dec. (J2000)	UT Dates	Exp. Time[a] (hr)	S/N (σ)	z	Y_{500} (10^{-5} Mpc^2)	r_{500} (Mpc)	M_{500} (10^{14} $M_\odot$)
MOO J0037+3306	00:37:45.8	+33:06:51	2014 Sep 12,27-28	6.0	3.3	1.133	$1.78^{+0.87}_{-0.73}$	$0.62^{+0.05}_{-0.06}$	$2.26^{+0.62}_{-0.61}$
MOO J0105+1323[e]	01:05:31.5	+13:23:55	2014 Jul 6; Oct 11	7.3	8.1	1.143	$1.49^{+0.91}_{-0.80}$	0.72 ± 0.03	$3.92^{+0.46}_{-0.44}$
MOO J0123+2545	01:23:50.3	+25:45:31	2014 Sep 27	1.9	4.4	1.224	$4.47^{+1.76}_{-1.43}$	0.70 ± 0.05	$3.86^{+0.85}_{-0.79}$
MOO J0319−0025[b]	03:19:24.4	−00:25:21	2013 Sep 30	1.0	5.7	1.194	$2.97^{+0.75}_{-0.78}$	$0.65^{+0.03}_{-0.04}$	$2.97^{+0.75}_{-0.78}$
MOO J1014+0038[b]	10:14:08.4	+00:38:26	2013 Oct 6-7	2.2	8.0	1.231	$3.34^{+0.64}_{-0.52}$	0.66 ± 0.02	$3.22^{+0.36}_{-0.31}$
MOO J1111+1503	11:11:42.6	+15:03:44	2014 Jul 23,25	4.4	5.0	1.32[d]	$1.58^{+0.41}_{-0.37}$	0.54 ± 0.04	$2.02^{+0.30}_{-0.30}$
MOO J1142+1527[c]	11:42:45.1	+15:27:05	2014 Jul 3	5.0	10.4	1.189	$7.70^{+1.36}_{-1.17}$	0.79 ± 0.03	$5.36^{+0.55}_{-0.50}$
MOO J1155+3901[b]	11:55:45.6	+39:01:15	2012 May 11-12	7.2	2.9	1.009	$2.05^{+0.72}_{-0.65}$	$0.66^{+0.04}_{-0.05}$	$2.53^{+0.50}_{-0.51}$
MOO J1231+6533	12:31:14.8	+65:33:29	2014 Sep 7-8	1.5	4.3	0.99[d]	$5.76^{+2.83}_{-1.80}$	$0.81^{+0.07}_{-0.06}$	$4.69^{+1.27}_{-0.94}$
MOO J1514+1346[b,e]	15:14:42.7	+13:46:31	2013 Jun 1,3,5-7,9,11	8.4	2.8	1.059	$1.91^{+0.73}_{-0.97}$	$0.63^{+0.04}_{-0.08}$	$2.39^{+0.51}_{-0.83}$
MOO J1521+0452	15:21:04.6	+04:52:08	2014 Sep 23	2.5	2.7	1.312	$4.13^{+2.14}_{-1.61}$	0.66 ± 0.07	$3.59^{+1.02}_{-0.92}$
MOO J2206+0906[e]	22:06:28.6	+09:06:32	2014 Jul 5,8	5.7	3.1	0.926	$2.58^{+1.30}_{-0.92}$	0.71 ± 0.06	$2.95^{+0.82}_{-0.68}$

[a]On-source, unflagged.

[b]Brodwin et al. (2015), with a mass and radius re-calculated from an improved CARMA reduction pipeline.

[c]Gonzalez et al. (2015), with a mass and radius re-calculated from an improved CARMA reduction pipeline and using a slightly different cosmology.

[d]Photometric redshift estimated from IRAC 3.6 μm and 4.5 μm images, with error ~ 0.07.

[e]Identified as a merging cluster from follow-up *Chandra* imaging (see Gonzalez et al., 2019).

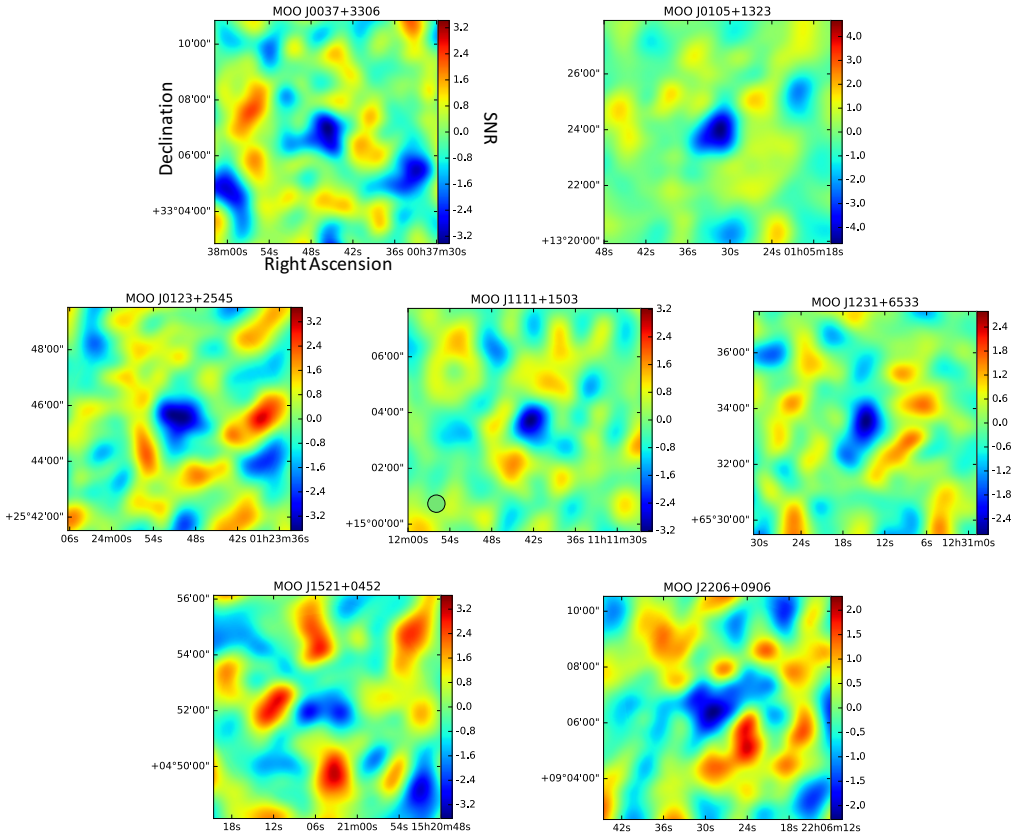

Figure 2 CARMA maps of the seven new MaDCoWS clusters presented here. Each map is $8' \times 8'$, centered on the centroid of the SZ decrement and in units of signal-to-noise. Emissive point sources have been subtracted out of all the maps and they have all been CLEANed around the decrement. A representative beam pattern is shown in the lower left-hand corner of the map of MOO J1111+1503.

2.2.2 Spitzer Data

Eight of the MaDCoWS clusters were observed in *Spitzer* Cycle 9 (Program ID 90177; PI Gonzalez) and have 6×30 s depth in the IRAC 3.6 μm and 4.5 μm channels, while the remaining four were observed to the same depth as part of a Cycle 11-12 snapshot program (PID 11080; PI Gonzalez). This depth allows us to detect objects down to one magnitude fainter than the characteristic magnitude (m^*) on all of our clusters with high ($> 70\%$) completeness. The SPT clusters were observed with *Spitzer* over four Cycles (PID 60099, 70053, 80012, 10101; PI Brodwin) to a depth of 8×100 s in 3.6 μm and 6×30 s in 4.5 μm.

2.2.3 Optical Data

Five of the MaDCoWS clusters have follow-up r- and z-band imaging with the Gemini Multi-Object Spectrograph (GMOS, Hook et al., 2004) on Gemini-North with five 180 s exposures in the r-band and twelve 80 s exposures in the z-band from programs GN-2013A-Q-44 and GN-2013B-Q-8 (PI Brodwin). The data were taken between 2013 February and 2015 July.

2.2.4 New Spectroscopic Redshifts

Five of the MaDCoWS clusters presented here have previously unreported spectroscopic redshifts. We obtained spectroscopic observations of these five clusters from 2015 through 2017, primarily with the Low Resolution Imaging Spectrometer (LRIS, Oke et al., 1995) at the W. M. Keck Observatory, the details of which are given in Table 2. The mask used for each cluster was designed from the *Spitzer*

imaging and focused on the IRAC sequence members identified in a 3.6 μm$-$4.5 μm color-magnitude diagram.

One of the clusters with new spectroscopic redshifts reported here, MOO J1521+0452, is the highest-redshift MaDCoWS cluster with spectroscopy, and with $M_{500} = (3.59^{+1.02}_{-0.92}) \times 10^{14}\ M_{\odot}$, it is the third-most massive cluster to be found at $z \geq 1.3$ by any method. The spectroscopy confirmed six cluster members and established $z = 1.312$ as the cluster redshift. Representative spectra of two of the confirmed members are shown in Figure 3.

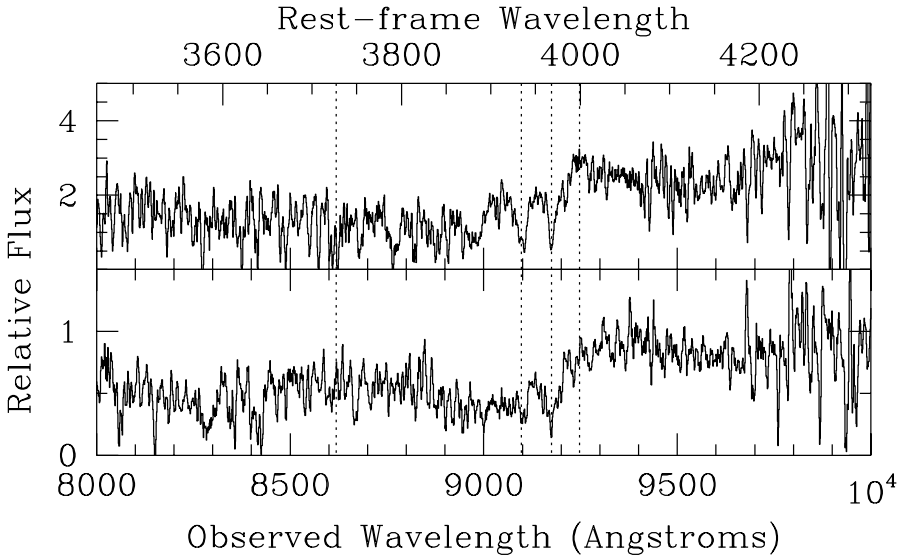

Figure 3 Spectra of two of the six confirmed members of MOO J1521+0452 at $z = 1.31$. The vertical lines show , left-to-right the locations of [O II] λ3727, Ca II K & H lines and D4000.

Four cluster members were confirmed for MOO J0037+3306, establishing the cluster redshift of $z = 1.133$. MOO J0105+1323 and MOO J0123+2545 each

had five identified members, placing their redshifts at $z = 1.143$ and $z = 1.215$, respectively.

In addition to the newly reported clusters above, we also present a new spectroscopic redshift for MOO J1014+0038, previously reported at a photometric redshift of $z_{\rm phot} = 1.27 \pm 0.08$ (Brodwin et al., 2015). In addition to LRIS spectroscopy, we also observed this cluster with the Multi-Object Spectrometer For Infra-Red Exploration (MOSFIRE, McLean et al., 2010, 2012) at Keck on 2016 February 01. These new spectra identified seven members and established the redshift for MOO J1014+0038 as $z = 1.231$. Spectra for two of these members are shown in Figure 4.

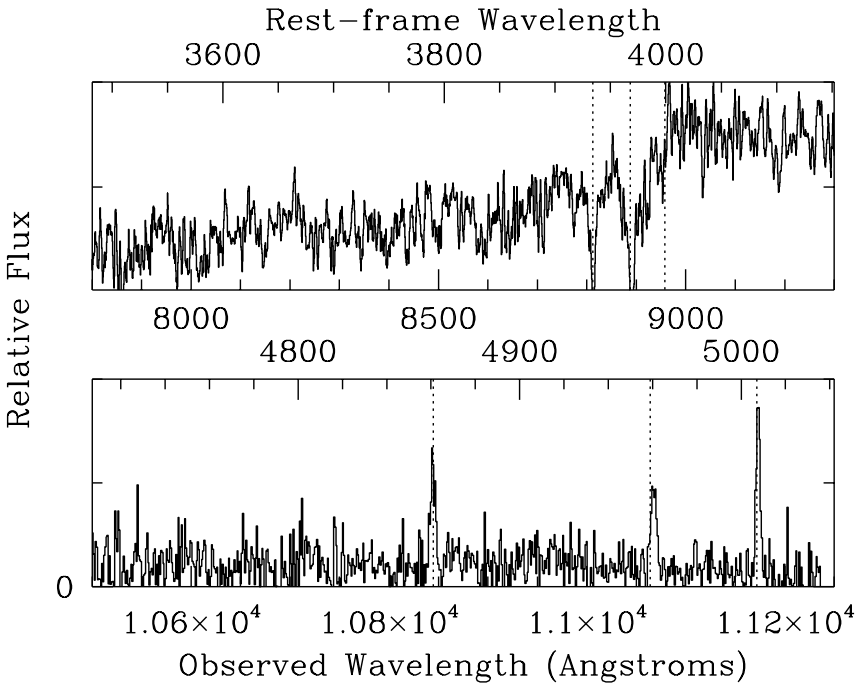

Figure 4 Spectra of confirmed MOO J1014+0038 cluster members from LRIS (top) and MOSFIRE (bottom), establishing a cluster redshift of $z = 1.231$. Left-to-right, the vertical lines of the top spectrum show the Ca II K&H lines and the 4000 Å break and the vertical lines of the lower plot show the Hβ and [O III] emission features.

Table 2. Spectroscopic Cluster Members

RA	Dec.	Instrument	UT Date	z	Quality[a]	Features
MOO J0037+3306 $z = 1.133$						
00:37:45.77	+33:07:50.9	LRIS	2016 August 05	1.131	A	D4000
00:37:46.18	+33:07:28.2	LRIS	2016 August 05	1.123	A	Ca HK
00:37:48.82	+33:07:08.4	LRIS	2016 August 05	1.15	B	D4000
00:37:47.03	+33:06:45.7	LRIS	2016 August 05	1.13	B	D4000
MOO J0105+1323 $z = 1.143$						
01:05:26.64	+13:23:36.9	LRIS	2015 December 04	1.13	B	D4000
01:05:26.20	+13:23:53.7	LRIS	2015 December 04	1.14	B	D4000
01:05:29.95	+13:23:54.6	LRIS	2015 December 04	1.15	A	Ca HK,D4000
01:05:35.27	+13:23:10.4	LRIS	2015 December 04	1.144	B	[O II]λ3727,D4000
MOO J0123+2545 $z = 1.215$						
01:23:50.95	+25:45:47.19	LRIS	2017 July 20	1.20	B	D4000
01:23:57.16	+25:44:16.67	LRIS	2017 July 20	1.22	B	D4000
01:23:47.37	+25:46:50.65	LRIS	2017 July 20	1.2214	A	[O II]λ3727
01:23:41.53	+25:47:32.78	LRIS	2017 July 20	1.2196	B	[O II]λ3727
MOO J1014+0038 $z = 1.231$						
10:14:07.31	+00:38:27.1	LRIS	2015 February 21	1.231	B	Ca HK
10:14:10.51	+00:37:56.2	LRIS	2015 February 21	1.23	B	D4000
10:14:08.11	+00:37:36.6	LRIS	2015 February 21	1.239	A	Ca HK
10:14:00.32	+00:36:43.7	LRIS	2015 February 21	1.22	B	[O II]λ3727
10:14:08.13	+00:38:21.3	LRIS	2015 December 06	1.23	B	Ca HK,D4000
10:14:12.80	+00:38:12.2	MOSFIRE	2016 February 01	1.2318	A	Hβ,[O III]λ4959,5007
10:14:09.71	+00:41:11.1	LRIS	2016 March 06	1.226	B	[O II]λ3727
MOO J1521+0452 $z = 1.312$						
15:21:13.66	+04:53:28.0	LRIS	2016 July 05	1.308	B	Ca HK
15:21:12.10	+04:51:16.9	LRIS	2016 July 05	1.317	B	Ca HK

Table 2 (cont'd)

RA	Dec.	Instrument	UT Date	z	Quality[a]	Features
15:21:06.79	+04:52:09.1	LRIS	2016 July 05	1.312	B	Ca HK,D4000
15:21:04.90	+04:51:59.8	LRIS	2016 July 05	1.302	B	Ca HK,D4000
15:21:04.15	+04:52:12.4	LRIS	2016 July 05	1.32	B	Ca HK,D4000
15:20:59.35	+04:51:40.7	LRIS	2016 July 05	1.314	A	Ca HK,D4000
Foreground/Background Objects						
00:37:51.56	+33:10:07.0	LRIS	2016 August 05	1.453	A	[O II]λ3727,D4000
01:05:22.72	+13:23:55.2	LRIS	2015 December 04	0.229	A	[O II]λ3727
01:05:35.14	+13:23:36.9	LRIS	2015 December 04	0.248	A	[O II]λ3727,Hα,Hβ
01:23:48.16	+25:46:01.2	LRIS	2017 July 20	0.2120	A	Hα,Hβ
01:23:42.28	+25:46:31.4	LRIS	2017 July 20	0.4659	A	Hα,[O III]λ4959,5007
01:23:42.32	+25:47:17.5	LRIS	2017 July 20	0.4364	A	Hα
01:23:56.71	+25:46:31.7	LRIS	2017 July 20	1.4781	A	[O II]λ3727,Ca HK
10:14:11.57	+00:38:39.3	LRIS	2015 February 21	1.158	A	Ca HK,D4000
10:14:02.48	+00:34:53.0	LRIS	2015 February 21	0.326	A	Hα
10:14:13.36	+00:39:57.8	LRIS	2015 December 06	0.966	A	Ca HK,D4000,G
10:14:04.15	+00:41:03.5	LRIS	2015 December 06	0.981	A	[O II]λ3727, Ca HK,D4000
10:14:00.76	+00:40:23.2	LRIS	2015 December 06	0.3283	A	Hα,[N II],Na D
15:21:08.78	+04:52:59.5	LRIS	2016 July 05	0.514	A	Hα,[N II]
15:20:52.34	+04:51:32.0	LRIS	2016 July 05	0.489	A	Hα,[N II]

[a]Qualities 'A' and 'B' denote redshifts of high and reasonable certainty, respectively (Stanford et al., 2014).

2.3 Analysis

2.3.1 Total Cluster Mass

Details of the CARMA observations are given in Table 1. The data, including those for clusters previously reported in Brodwin et al. (2015) and Gonzalez et al. (2015), were re-reduced using a new MATLAB pipeline designed specifically for CARMA data. Mars was used as the flux calibrator for each cluster with the Rudy et al. (1987) flux model and observations of a bright monochromatic quasar were interleaved with

the cluster observations for gain calibration. The cluster Comptonization ($Y_{\rm SZ}$) was calculated by using a Monte Carlo Markov Chain to fit an Arnaud et al. (2010) pressure profile and point source models (where indicated by the long baseline data) to the CARMA data in *uv* space. The significance of the detection was calculated by comparing χ^2 for the fit to the Arnaud model and point source(s) to χ^2 for a fit to just the point source(s) with no cluster model. M_{500} and r_{500} were calculated from Y_{SZ} by forcing consistency with the scaling relation from Andersson et al. (2011). The resulting masses, radii and Y_{SZ} values are shown in Table 1. Updated masses and radii, based on the new pipeline, are reported for the clusters reported in Brodwin et al. (2015) and Gonzalez et al. (2015). These are all consistent within one sigma with the originally reported quantities. The total masses for the SPT-SZ sample are from the Bleem et al. (2015) catalog.

2.3.2 Catalogs

For each cluster we ran SExtractor (Bertin & Arnouts, 1996) in dual-image mode on the 3.6 μm and 4.5 μm images, selecting on the 3.6 μm image. We used the IRAC coverage maps as weights and SExtractor parameters similar to those in Lacy et al. (2005). These parameters are optimized for IRAC, but we changed DEBLEND_NTHRESH to 64 and DEBLEND_MINCONT to 0.00005 to better deblend sources in the cluster cores. Magnitudes were measured in 4″ diameter apertures and corrected to 24″ diameter apertures using the corrections from Ashby et al. (2009).

Catalogs for the optical images were produced with the same SExtractor parameters, but with MAG_AUTO magnitudes instead of corrected aperture magnitudes. The optical and infrared catalogs were then matched using the IRAC astrometry to produce combined catalogs for each cluster. All of the catalogs have IRAC 3.6 μm and 4.5 μm fluxes that are $\gtrsim 70\%$ complete down to magnitudes of 21.0 and 22.5, respectively. The clusters with optical data have additional r- and z-band data similarly complete to depths of 25.5 and 24.5 magnitudes.

2.3.3 Cluster Membership

Because our cluster masses are measured at an overdensity of $\Delta = 500$, we only consider galaxies projected within r_{500} (as determined from the SZ data) from the centroid of the SZ decrement in our measurement of stellar masses and fractions (e.g., Figure 5). To ensure our choice of center does not significantly impact our results, we also ran our analysis using the centroid of the galaxy distribution and using the BCG as the center. We find no appreciable differences in our results. Within r_{500}, we also reject objects that likely lie in the foreground by not including any source with an apparent magnitude brighter than $m^* - 2$ at the redshift of our cluster. The effects of this choice of cutoff are discussed in §2.5.4. The characteristic magnitude was calculated using the same model as was used for our K-corrections (described in §2.4.1). To limit the effect of incompleteness at the faint-end, we reject objects more than one magnitude fainter than m^*.

We used the available optical data for five of the MaDCoWS clusters to

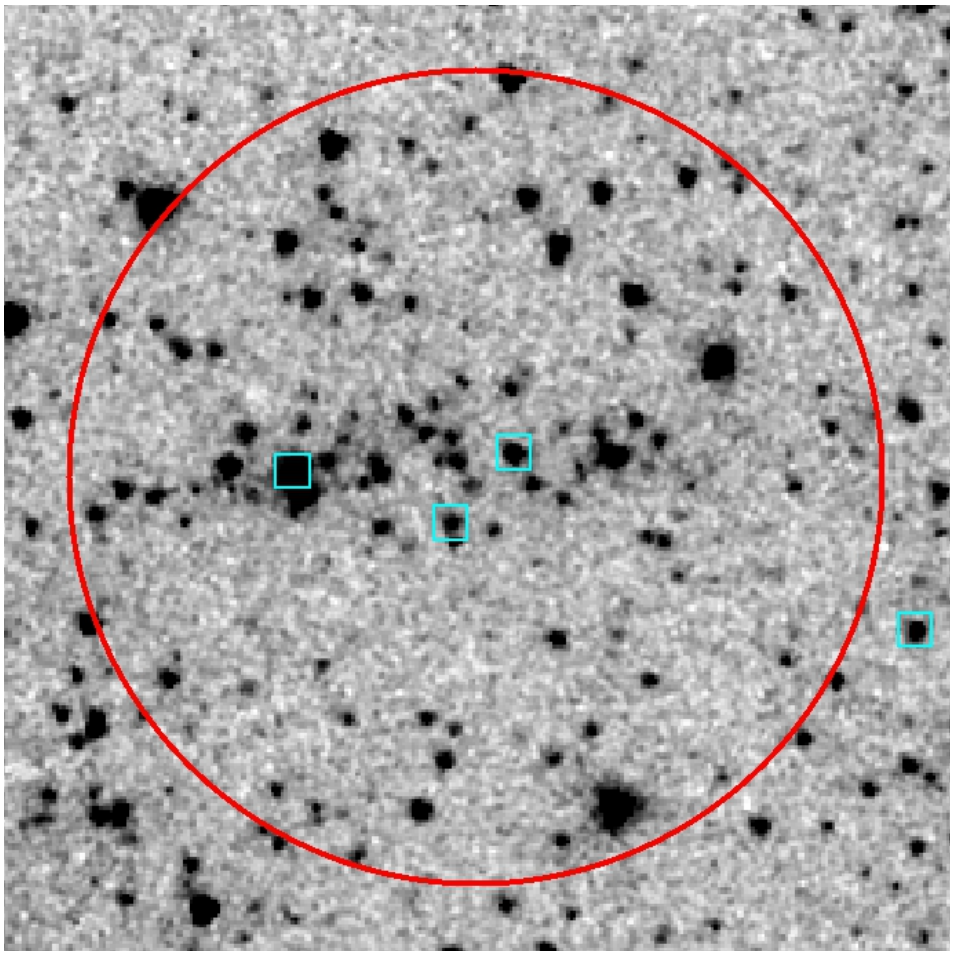

Figure 5 A $170'' \times 170''$ *Spitzer*/IRAC 3.6 μm image of MOO J1521+0452 showing an $80''$ radius circle corresponding to the cluster r_{500} of 0.67 Mpc at $z = 1.31$. Only galaxies inside the red circle were included in the analysis. Cluster members with spectroscopic redshifts are marked with cyan squares.

identify stars in color-color space. Following Eisenhardt et al. (2004), we plot $r - z$ versus $z{-}3.6$ μm colors for each of our possible cluster members. To the limit where our optical data are complete for all clusters, we characterize as stars objects falling above the line shown in Figure 6 that separates objects with the colors of stars from objects that are likely galaxies. Only objects bright enough to be clearly detected in even the shallowest of our optical images are so characterized to ensure a consistent cut across all clusters. We also match our catalogs to objects in the *Gaia* DR2 catalog (Gaia Collaboration et al., 2016, 2018) with greater than 3 σ parallax, to confirm that objects known to be stars are the objects being rejected by this approach. We cannot do this for the SPT clusters due to a lack of comparable optical data.

Although the bulk of galaxies within r_{500} are cluster members, there is still a line-of-sight interloper contribution that must be subtracted. To account for this, we determine the expected contribution to the total flux density from field galaxies within the projected r_{500} area and subtract it off the flux density calculated from our cluster. We use the *Spitzer* Deep Wide-Field Survey (SDWFS, Ashby et al., 2009) to do this, applying the same brightness cuts to reject non-cluster members as we apply to our cluster catalogs. For the clusters with optical data allowing the rejection of stars, we use optical photometry from the NOAO Deep Wide-Field Survey (NDWFS, Jannuzi & Dey, 1999) to make the analogous stellar rejection in our background. For each cluster, we treat all remaining objects in the SDWFS catalog as though they were at the redshift of that cluster and calculate how much spurious luminosity they

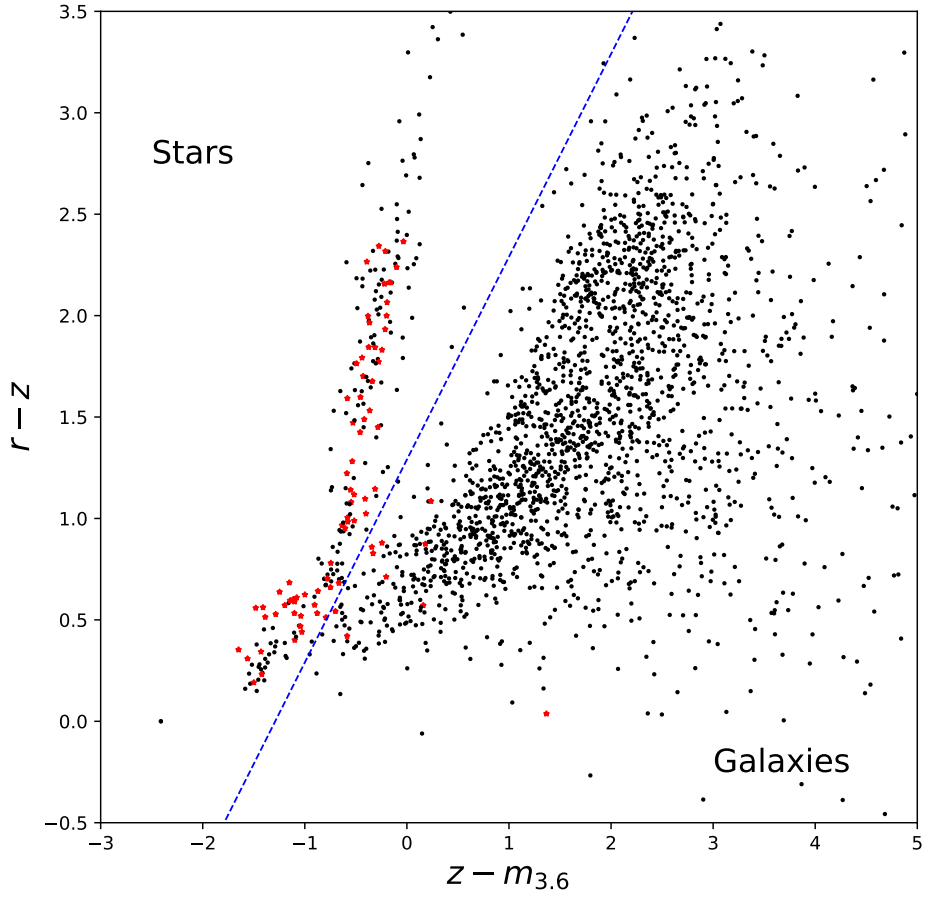

Figure 6 Combined color-color plot of all the MaDCoWS clusters for which there are GMOS data, showing $r - z$ color plotted against $z - m_{3.6}$. Objects above the blue dashed line have colors consistent with being stars. Objects with $\geq 3\ \sigma$ parallax in the *Gaia* DR2 catalog are plotted as red stars.

would add. We use the SDWFS field to determine our background because the IRAC imaging is deeper than that of our clusters and because SDWFS is large enough to smooth out small-scale variations in the background level. This background selection methodology does produce an appreciable systematic uncertainty in our results, as discussed in §2.5.4.

2.3.4 Completeness

To correct for incompleteness in our IRAC catalogs, we ran completeness simulations over the range of magnitudes at which we were looking using IRAF's *mkobjects* task in the *noao/artdata* package. For each cluster we added ten random point sources in each half magnitude bin to the IRAC 3.6 μm image, and ran SExtractor to see how many were recovered. We repeated this process 1,000 times in each magnitude bin. This was done for both the MaDCoWS and SPT clusters and we performed a similar analysis on the SDWFS 3.6 μm image and on the optical images of the clusters. The average completeness curve for MaDCoWS and SPT are shown in Figure 7. At $m^* + 1$, the faint-end limit of our analysis, the catalogs of both surveys are approximately 70% complete, depending slightly on cluster redshift. Because our clusters have slightly different m^* (depending on redshift), our faint-end cutoff varies slightly, as shown in the figure.

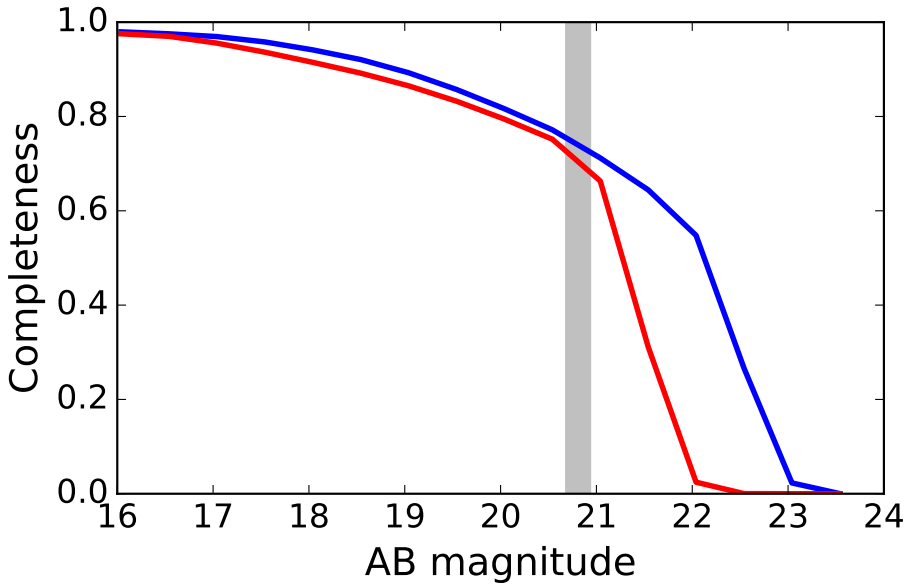

Figure 7 Average completeness curves for the MaDCoWS (red) and SPT (blue) IRAC 3.6 μm images in AB magnitudes. The shaded region represents the range of maximum depths to which our analysis extends.

2.4 Results

2.4.1 Stellar Mass

We calculate the stellar mass of the galaxies selected as possible cluster members using their rest-frame H-band luminosity. The rest frame H-band is centered at the peak of the emission from the old, red stars that dominate the stellar mass of the galaxy. It is therefore a relatively low-scatter proxy for total stellar mass (e.g., Hainline et al., 2011) with a relatively small dependence on the overall SED. At $z \sim 1$ this is easily probed by the IRAC 3.6 μm band. To determine the K-correction from observed IRAC 3.6 μm to rest-frame H-band, we use EZGal (Mancone & Gonzalez, 2012). We construct a synthetic galaxy SED with a Bruzual & Charlot (2003) 1 Gyr tau model, formation redshift $z_{\rm f} = 3$, solar metallicity and a Chabrier (2003) IMF. From this SED we derive a K-correction to the absolute magnitude in the H-band, from which we calculate $L_{\rm H}$. We statistically correct our luminosities for incompleteness using the simulations described above. We use the same EZGal model to determine the stellar mass-to-light ratio in the H-band at the cluster redshift. This M/L ratio is different for each cluster, depending on the redshift, but is close to 0.34 on average. We apply the stellar M/L ratio to the sum of the luminosities of all the objects along the line of sight minus the background contribution estimated from SDWFS to get our final cluster stellar mass. Both the MaDCoWS and SPT clusters were analyzed in the same way and to the same depth to allow for direct comparison of the two samples.

2.4.2 Estimating Stellar Corrections with Luminosity Functions

Before calculating total stellar mass fractions, we need to account for foreground stars along the line-of-sight to our clusters. We do this by combining the optical stellar identification discussed above with cluster luminosity functions to estimate and correct the total impact from stars on our clusters that lack optical data.

The mean IRAC 3.6 μm luminosity function (LF) for the five MaDCoWS clusters with optical data for stellar rejection is shown in Figure 8. To make this LF we applied the membership cuts from §3.3.1, including stellar rejection from the optical data, to each cluster and evolution-corrected the members to $z = 1$. The galaxies from all the clusters were then binned in quarter-magnitude wide bins and the appropriate completeness and statistical background corrections were applied. The uncertainties on the values are Poisson errors.

We fit to the data a parameterized Schechter function of the form

$$\Phi(m) = 0.4\ln(10)\Phi^* 10^{-0.4(m-m^*)(\alpha+1)}\exp(-10^{-0.4(m-m^*)})$$

(Schechter, 1976) and we fix $\alpha = -0.8$ as our data are not deep enough to constrain the faint-end slope. This choice is consistent with Mancone et al. (2010) and is a reasonable value for our data. The best-fit value is $m^* = 19.41 \pm 0.07$ and we take this LF as representative of $z = 1$ clusters independent of selection. The error on the m^* fit is calculated from the range of χ^2, and is the same as the error calculated from bootstrap resampling. This value for m^* is slightly lower than, but close to that of Muzzin et al. (2008) who found $m^*_{3.6} = 20.11 \pm 0.64$ (in AB magnitudes) for

IRAC 3.6 μm at $z = 1.01$ and Mancone et al. (2010) who found $m^*_{3.6} = 19.71 \pm 0.06$ at $z = 0.97$. It is also consistent with the value of $m^*_{3.6} = 19.62^{+0.25}_{-0.20}$ found for infrared-selected clusters in a higher redhift bin ($z = 1.45$) by Wylezalek et al. (2014).

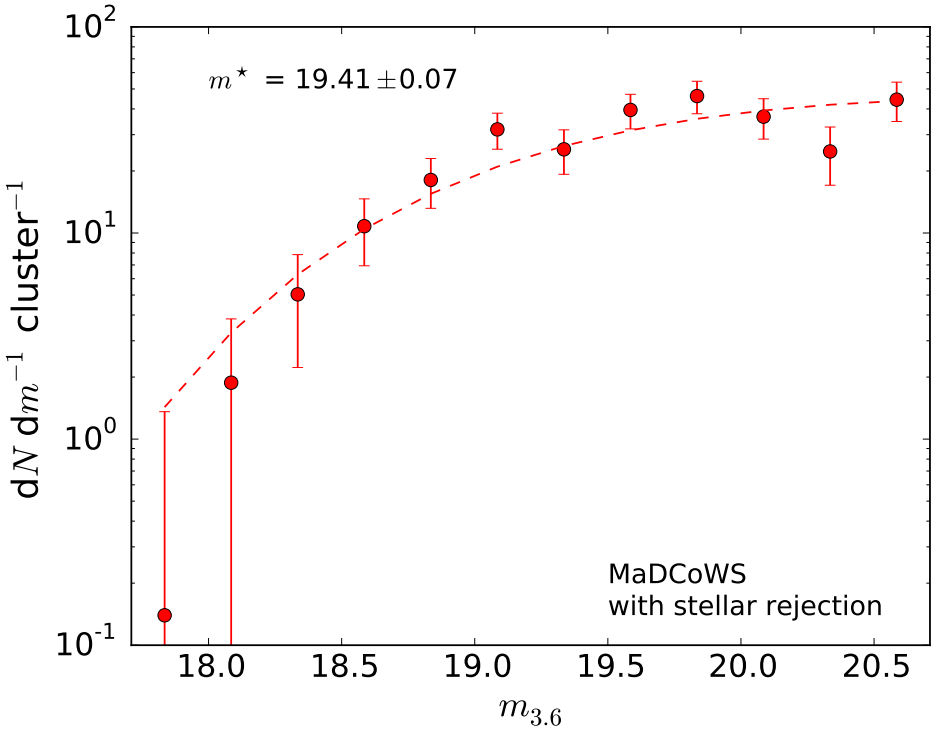

Figure 8 The IRAC 3.6 μm luminosity function for the five MaDCoWS clusters with optical data for stellar rejection. The solid circles are background subtracted number per magnitude in each bin and the error bars are from Poisson noise. The dashed line is a best-fit Schechter function with a fixed $\alpha = -0.8$ and the best-fit value of m^* is shown.

We used a similar approach to make luminosity functions for the full sample of twelve MaDCoWS clusters and for the SPT clusters, shown in Figures 9 and

10, respectively. The stellar contamination is more extensive for the SPT clusters because the sample extends to a lower galactic latitude, where there is more line-of-sight contamination, than does the MaDCoWS sample. We do not have adequate optical data for all of these clusters and thus do not attempt stellar corrections on a per-cluster basis. Rather, we construct a statistical stellar correction as follows. We fit the $z = 1$ Schechter function determined above, allowing only Φ^* to vary (i.e., with fixed $\alpha = 0.8$ and $m^* = 19.41$ as for the clusters without stellar contamination), to the points at the faint end of MaDCoWS and SPT LFs that show no evidence of stellar contamination (as determined by the SPT LF). These are the points plotted with filled circles in Figures 9 and 10; the unfit portion of the LFs, where there appears to be significant stellar contamination in the SPT LF, is plotted with black crosses. The ratios between the areas under these 'no-stars' fits for each sample, over the full magnitude range in this work, to the area under their respective observed LFs is the statistical stellar correction factor for that sample. We multiply the measured luminosity of each cluster by the correction factor of the sample to get the true luminosity for that cluster absent stellar contamination.

2.4.3 Stellar Mass Fraction

To calculate $f_\star$, we divide the stellar mass of the cluster by the total mass calculated from the SZ decrement described above. The stellar mass that we use is calculated by summing the completeness- and K-corrected H-band luminosity of every object projected within r_{500} of the cluster SZ centroid and subtracting the

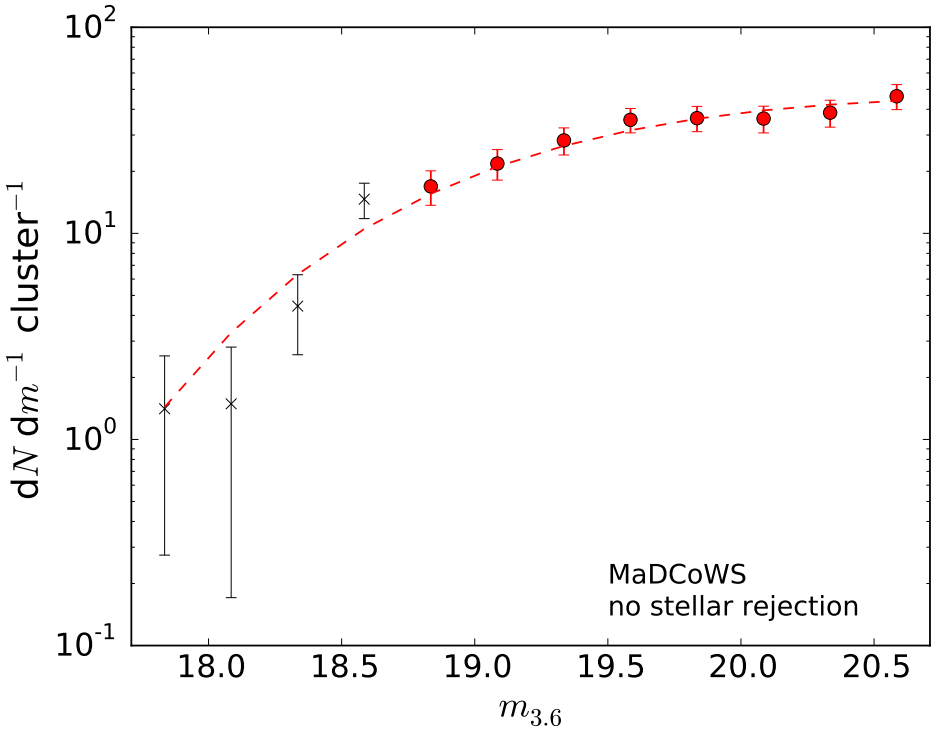

Figure 9 The mean IRAC 3.6 μm luminosity function for the full sample of twelve MaDCoWS clusters with no optical rejection of stars. All of the points are background-subtracted number per magnitude in each bin and the error bars are from Poisson noise. The black crosses on the bright end are points with potential stellar contamination that we did not include when fitting the Schechter function, which is represented by the dashed red line. For the Schechter function, we fixed $\alpha = -0.8$ and $m^* = 19.41$ to match the luminosity function derived using optical stellar rejection.

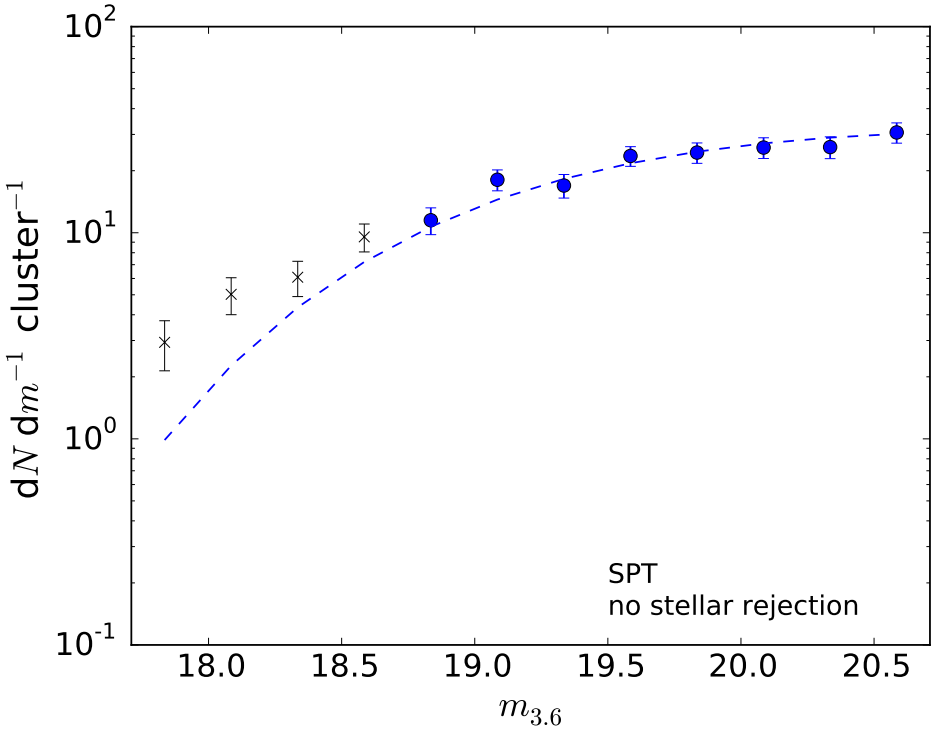

Figure 10 The mean IRAC 3.6 μm luminosity function for the 33 comparison SPT clusters in this work. All of the points are background-subtracted number per magnitude in each bin and the error bars are from Poisson noise. The black crosses on the bright end are points with likely stellar contamination that we did not include when fitting the Schechter function, which is represented by the dashed blue line. For the Schechter function, we fixed $\alpha = -0.8$ and $m^* = 19.41$ to match the MaDCoWS LF. Note the stellar contamination at the bright end.

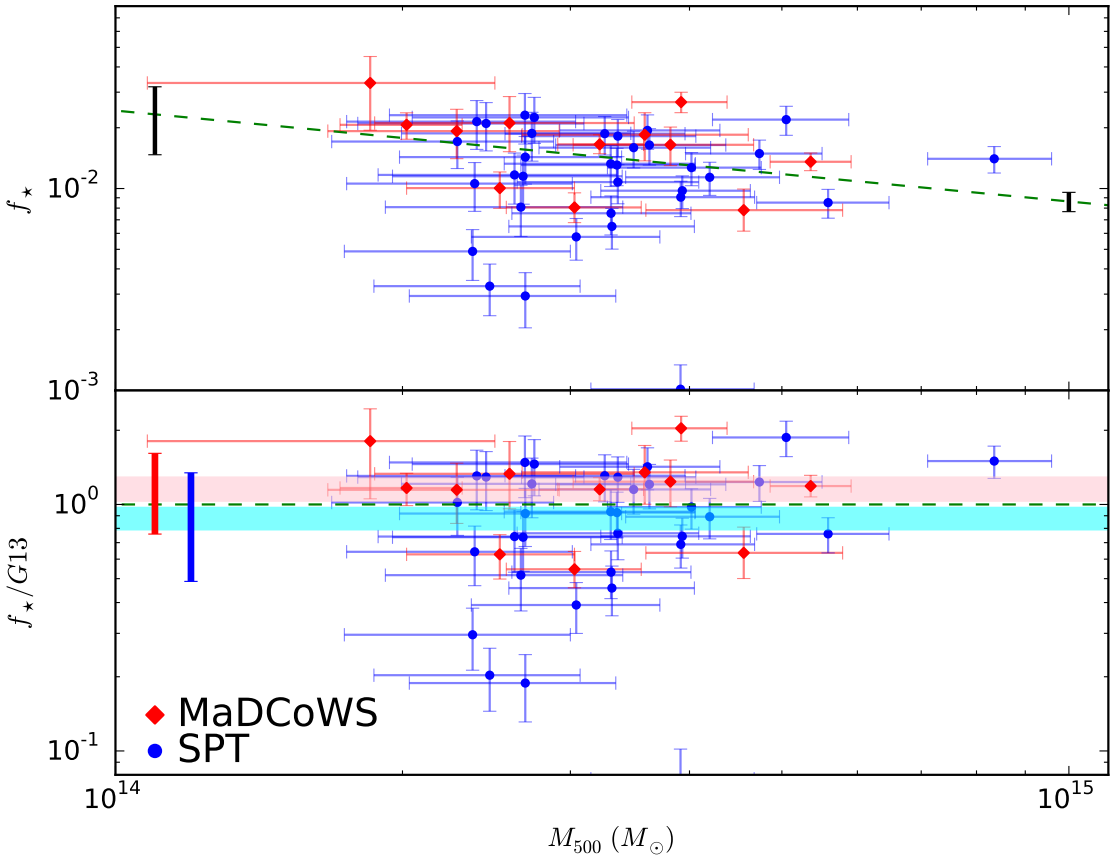

Figure 11 *Upper*: Stellar mass fraction versus total mass for the MaDCoWS (red) and SPT (blue) clusters. The size of the systematic error in $f_\star$, which varies with M_{500}, is represented by the black error bars on either end of the figure. The green dashed line is the low-redshift relation from G13. *Lower*: The stellar mass fractions of each cluster normalized by the G13 relation versus total mass. The error about the mean normalized $f_\star$ for both samples is calculated from bootstrap resampling and for MaDCoWS (SPT) is plotted in pink (cyan) across the figure. The scatter in normalized $f_\star$ is shown by the thick, vertical red (blue) error bars.

average background calculated from SDWFS. We then multiply this luminosity by the M/L ratio from our EZGal model for the cluster redshift and the average stellar correction for either the MaDCoWS or SPT subsample calculated above. The systematic uncertainties inherent in this method are discussed in §2.5.4.

A plot of $f_\star$ versus M_{500} is shown in the upper panel of Figure 17, in which the red diamonds represent the infrared-selected MaDCoWS clusters and the blue circles represent the SZ-selected SPT clusters. The dashed green line is the low-redshift relation found by Gonzalez et al. (2013, hereafter G13) and the black error bars on either side of the plot indicate the systematic error introduced by the background subtraction. For each cluster in both samples the stellar mass fraction was calculated without any stellar rejection and then the average stellar correction for the appropriate sample, as described in §2.4.2, was applied in order to achieve a consistent stellar correction for all the clusters in each sample.

On average, the MaDCoWS clusters do not have significantly higher stellar mass fractions than the SPT clusters. There is a sizable systematic error, largely from the background subtraction, which is both larger than the statistical error and mass dependent, but it should affect both samples to the same degree and thus does not affect the direct comparison. This is dicussed further in §2.5.4. To ensure that this comparison of $f_\star$is unrelated to the trend of $f_\star$ with mass seen at low redshift, we also divide out the G13 trend line, as shown in the lower half of Figure 17. The errors on the resulting G13-normalized means for each sample are calculated from bootstrap resampling and shown as horizontal pink and cyan bars across the data.

Table 3. MaDCoWS Stellar Mass Fractions

ID	z	M_{500} ($10^{14}\ M_\odot$)	$M_\star$ ($10^{12}\ M_\odot$)	$f_\star$ (10^{-2})
MOO J0037+3306	1.139	$2.28^{+0.64}_{-0.61}$	4.48 ± 0.15	$1.97^{+0.56}_{-0.53}$
MOO J0105+1323	1.143	$3.92^{+0.46}_{-0.44}$	10.73 ± 0.19	$2.74^{+0.32}_{-0.31}$
MOO J0123+2545	1.224	$3.82^{+0.85}_{-0.80}$	6.43 ± 0.16	$1.68^{+0.38}_{-0.35}$
MOO J0319−0025	1.194	$3.03^{+0.53}_{-0.46}$	2.50 ± 0.12	$0.82^{+0.15}_{-0.13}$
MOO J1014+0038	1.229	$3.22^{+0.36}_{-0.31}$	5.44 ± 0.16	$1.69^{+0.20}_{-0.17}$
MOO J1111+1503	1.32	$2.02^{+0.29}_{-0.30}$	4.27 ± 0.13	$2.11^{+0.31}_{-0.32}$
MOO J1142+1527	1.189	$5.36^{+0.55}_{-0.50}$	7.43 ± 0.18	$1.39^{+0.15}_{-0.13}$
MOO J1155+3901	1.009	$2.53^{+0.50}_{-0.51}$	2.60 ± 0.11	$1.03^{+0.21}_{-0.21}$
MOO J1231+6533	0.99	$4.56^{+1.23}_{-0.96}$	3.64 ± 0.12	$0.80^{+0.22}_{-0.17}$
MOO J1514+1346	1.059	$1.85^{+0.65}_{-0.77}$	6.30 ± 0.13	$3.40^{+1.20}_{-1.42}$
MOO J1521+0452	1.312	$3.59^{+1.02}_{-0.92}$	6.77 ± 0.17	$1.89^{+0.54}_{-0.49}$
MOO J2206+0906	0.951	$2.59^{+0.91}_{-0.72}$	5.58 ± 0.12	$2.16^{+0.76}_{-0.60}$

This normalization still does not show a significant difference between the mean of the twelve MaDCoWS clusters and the 33 SPT clusters, though there is still a relatively large error on the individual $f_\star$ errors for both sets of clusters. Stellar masses and stellar mass fractions for the MaDCoWS clusters are given in Table 5.

As the vertical red and blue error bars in the lower panel of Figure 17 show, the scatter in the SPT stellar mass fractions is larger than that of the MaDCoWS clusters. There is also a much larger range in the SPT stellar mass fractions, with an order of magnitude separating the highest $f_\star$ clusters from the lowest. The scatter

in $f_\star$ seen in the MaDCoWS clusters is lower, but may not be representative of the general cluster population because of two selection biases. First, MaDCoWS is a stellar mass-selected cluster sample. As such, it may be biased toward systems with higher-than-average $f_\star$ values. Second, this particular subset of MaDCoWS clusters consists of the most significant detections from the first stage of the study, so may not be representative of the sample or of clusters as a whole. We do not expect the different redshift distributions to introduce a bias, however, as we find no evidence that $f_\star$ evolves with redshift. The SPT clusters, however, should provide a fair sample of the mean value and scatter of the stellar mass fraction at the redshift of those SZ-selected clusters because they are selected independently of those components. We compared the stellar mass fractions of the MaDCoWS and SPT samples using a Kolmogorov-Smirnov test and found they were consistent with being drawn from the same underlying distribution.

The MaDCoWS sample contains three clusters known to be merging from high-resolution *Chandra X-ray Observatory* follow-up observations (Gonzalez et al., 2019). Previous studies of the effect merging has on the inferred Y_{SZ} mass of a cluster have produced mixed conclusions, with some (e.g., Poole et al., 2007; Krause et al., 2012) finding that major mergers bias the inferred Y_{SZ} mass of a system low for most of the observed timescale and others, (e.g., Marrone et al., 2012) finding the Y_{SZ} mass of merging clusters was overestimated. We do not expect merging to affect the observed richness of a cluster in the same way as the mass, however, so any effect on the inferred mass will bias our measurement of $f_\star$. We do not have X-ray data

for the full MaDCoWS sample or the comparison SPT sample, so we cannot fully remove mergers from our current analysis. However the effect of excluding these clusters, for which we know our $f_\star$ measurement is likely to be wrong, is shown in Figure 12. The clusters are plotted in the same manner as the lower part of Figure 17, however the three clusters known to be mergers are now plotted as open red diamonds and the mean is recalculated to exclude them. Although they are not large outliers, the three merging systems do have the highest normalized stellar mass fractions of the MaDCoWS sample. When they are excluded, the mean-normalized $f_\star$ for MaDCoWS decreases to $f_\star/G13 = 1.02 \pm 0.10$, still higher than that of the SPT clusters, but now consistent within 1 σ. We also removed two clusters from the SPT sample identified as mergers in Nurgaliev et al. (2017, shown as open circles) which did not affect the mean $f_\star/G13$ of the SPT clusters.

2.5 Discussion

2.5.1 Comparison of Stellar Mass Fractions

As discussed above, Figures 17 and 12 show that the average stellar mass fraction in the MaDCoWS sample is not significantly higher than that of the SPT sample, though there is considerable scatter. To confirm that this is not an artifact of the trend of $f_\star$ with mass we normalized all the $f_\star$ measurements relative to the G13 relation and measured the normalized mean $f_\star$ for both samples, shown in the lower panel of Figure 17. While the mean normalized $f_\star$ for MaDCoWS, $f_\star/G13 = 1.16 \pm 0.12$, is higher than the corresponding mean for the SPT sample, $f_\star/G13 =$

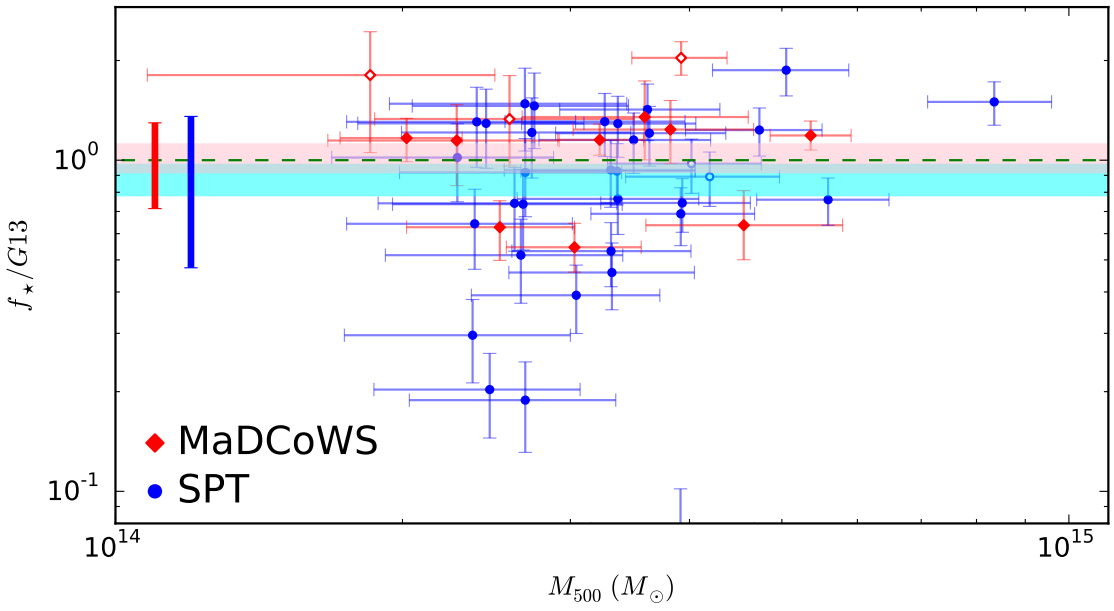

Figure 12 The same as the lower panel of Figure 17, with the merging MaDCoWS clusters (now shown as open diamonds) removed from the calculation of the mean normalized $f_\star$. The effect of removing these clusters for which the total mass is known to be underestimated relative to the stellar mass is to drop the G13-normalized mean to $f_\star/G13 = 1.02 \pm 0.10$, 1.0σ higher than the unchanged SPT mean.

0.88 ± 0.09, these are consistent within 1.9 σ.

2.5.2 Scatter in the Stellar Mass Fraction

The SZ-selected SPT clusters are best-suited to measure the scatter in $f_\star$ at high-redshift as they are selected independently of stellar content and thus should represent an unbiased sampling of the stellar mass fraction in the full cluster population. The large range in $f_\star$ seen in this sample, approximately an order of magnitude (see Figure 17), is perhaps surprising. As Figure 13 shows, however, this variation is clearly apparent in a visual inspection of the richnesses of two clusters with the same halo mass. Although both clusters in this figure have an SZ mass of M_{500} $= 2.7 \times 10^{14} M_\odot$ (Bleem et al., 2015), SPT-CL J0154-4824 (left) has a stellar mass fraction of $f_\star = (2.8 \pm 0.9) \times 10^{-3}$ whereas SPT-CL J2148-4843 (right) has a stellar mass fraction of $f_\star = (2.6 \pm 0.7) \times 10^{-2}$, an order of magnitude higher.

The MaDCoWS clusters in this work do not exhibit the same wide peak-to-trough range of stellar mass fractions nor as large a scatter, measured by the standard deviation of $f_\star$, presumably because they represent the high-richness end of an infrared-selected sample rather than a fair cross-section of all clusters. We attempt to quantify the *intrinsic* scatter in $f_\star$ of both samples about their respective means, independent of our measurement errors, by assuming that the reduced chi-squared will be equal to unity when all the errors are included in the error budget. We therefore set the reduced chi-squared for each sample to unity and solve for the intrinsic scatter term. We find a significant intrinsic scatter, $\sigma_{\ln f_\star} \sim 0.4$ dex for

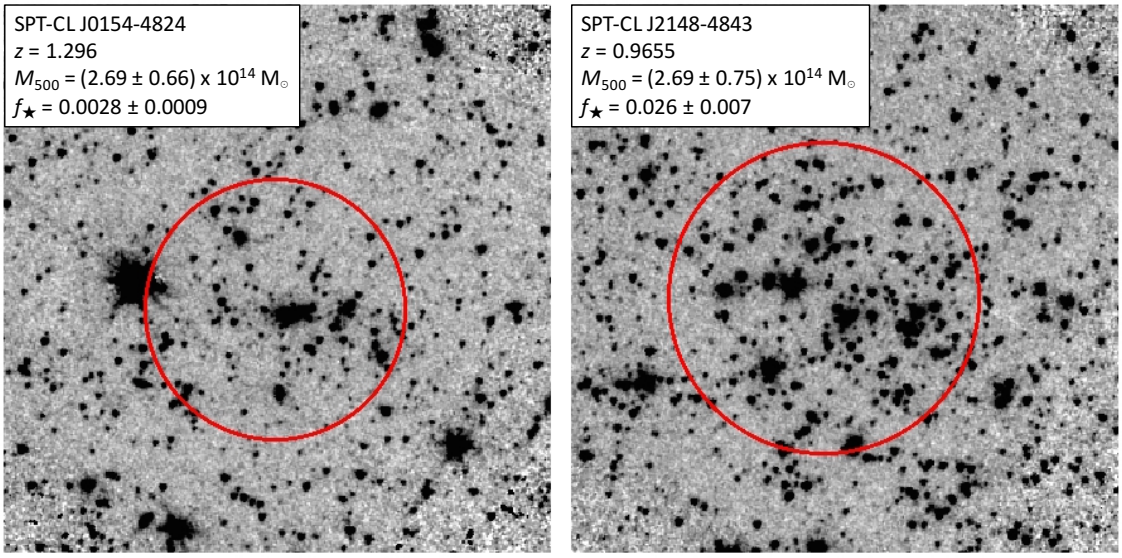

Figure 13 IRAC 3.6 μm images of SPT-CL J0154-4824 (left) and SPT-CL J2148-4843 (right) showing the large difference in richness between clusters of the same halo mass. The projected r_{500} of each cluster is shown as a red circle. The difference in the angular size of the two circles is due to the redshift difference, which boosts the richness by 28% in the nearer cluster, but the comparison is relatively unaffected by the differential K-correction between the clusters as m^* in *Spitzer* 3.6 μm is not significantly different between the two redshifts.

the SPT and $\sigma_{\ln f_\star} \sim 0.3$ dex for MaDCoWS. This discrepancy supports the idea described in §3.4.1, that the MaDCoWS clusters may not provide a fair measurement of the scatter in $f_\star$ due to their selection, but the SPT clusters should. By the same token, the MaDCoWS clusters should provide fair measurements of the scatter in $f_{\rm gas}$ that the SZ-selected surveys may not; this is a topic for future analyses with MaDCoWS. The SPT clusters show a larger intrinsic scatter in $f_\star$ than is predicted in simulations, such as those of Kravtsov et al. (2005), Ettori et al. (2006) and Planelles et al. (2013). Very recently, IllustrisTNG (Pillepich et al., 2017) directly measured the scatter in the stellar-total mass relationship in simulated clusters at $z = 0$ and $z \sim 1$ and found a very low scatter in the relationship, only 0.07 dex. Some of the low values and high scatter in the SPT $f_\star$ measurements may be due to the masses of low signal-to-noise clusters being overestimated. The clusters we use go to the low signal-to-noise limit of the SPT-SZ catalog and it is possible that some of these are lower mass clusters that scattered up above the cutoff. If we exclude these clusters, the intrinsic scatter of the SPT sample becomes consistent with that of the MaDCoWS clusters. This effect notwithstanding, understanding the baryonic processes causing the remaining large intrinsic scatter in stellar mass fraction, for which the MaDCoWS measurement of $\sigma_{\ln f_\star} \sim 0.3$ dex may be considered a lower limit, is a challenge for the next generation of cosmological simulations.

2.5.3 Comparison to Other Works

Given the systematic uncertainties described above, it is difficult to make direct comparisons to other works with different systematics. Nevertheless, other works with similar methodologies provide good external checks on our results, and in particular, allow us to test the effect of infrared- versus ICM-selection.

Chiu et al. (2018) also measured $f_\star$ for 84 clusters from the SPT-SZ survey, some of which overlap with our SPT comparison clusters. We do not expect to find the same $f_\star$ values for these clusters, as they use a slightly different cluster mass estimation (from de Haan et al., 2016) and an SED-fitting method to calculate stellar mass. Nevertheless, their average value for $f_\star$ is consistent with ours for the clusters in the same range of mass and redshift.

Hilton et al. (2013) reported stellar and total masses for a sample of 14 SZ-selected clusters from the Atacama Cosmology Telescope (ACT) in a redshift range of $0.28 \leq z \leq 1.06$. They have a mean stellar mass fraction of $f_\star = 0.023 \pm 0.003$, which is larger than what we find for our SZ-selected clusters. However, we use a Chabrier (2003) IMF to calculate stellar mass-to-light ratios which results in lower stellar masses than the Salpeter (1955) IMF Hilton et al. (2013) used. Accounting for the difference in stellar mass resulting from the choice of IMFs (0.24 dex), our results are consistent with theirs.

Similarly, van der Burg et al. (2014) reported stellar and halo masses for ten red sequence-selected clusters in a similar redshift range as ours. Using SED-fitting to determine the stellar mass of each galaxy, they find a mean stellar mass fraction

for their IR-selected clusters of $f_\star = 0.013 \pm 0.002$. This is consistent with our MaDCoWS mean of $f_\star = 0.015 \pm 0.005$, however their method of calculating stellar mass has different systematics to ours. Correcting for these, as described below, shifts their average stellar mass fraction higher than the MaDCoWS value, but it remains consistent with the G13 trend due to their lower mass range. When we divide out the G13 line in the same manner as in Figure 17, we find they have an average normalized stellar mass fraction of $f_\star/\mathrm{G13} = 0.98$, consistent with what we find for MaDCoWS.

Figure 14 shows $f_\star$ versus M_{500} for our MaDCoWS and SPT clusters plotted alongside the values found by the studies described above. To make a meaningful comparison, we corrected the Hilton et al. (2013) and van der Burg et al. (2014) results to a Chabrier IMF. We further corrected the latter for the offset between SED-fitted and M/L-based stellar masses reported in that work. The infrared-selected MaDCoWS and van der Burg et al. (2014) clusters are plotted as red and violet diamonds, and the SZ-selected SPT clusters in this work, the Chiu et al. (2018) SPT clusters and the Hilton et al. (2013) ACT clusters are plotted as blue, green and cyan circles, respectively. The SZ-selected studies again find broadly similar stellar mass fractions to the infrared-selected studies, consistent with what we find here. The G13 relation is plotted as a dashed line and for each sample error bars are plotted for three representative clusters.

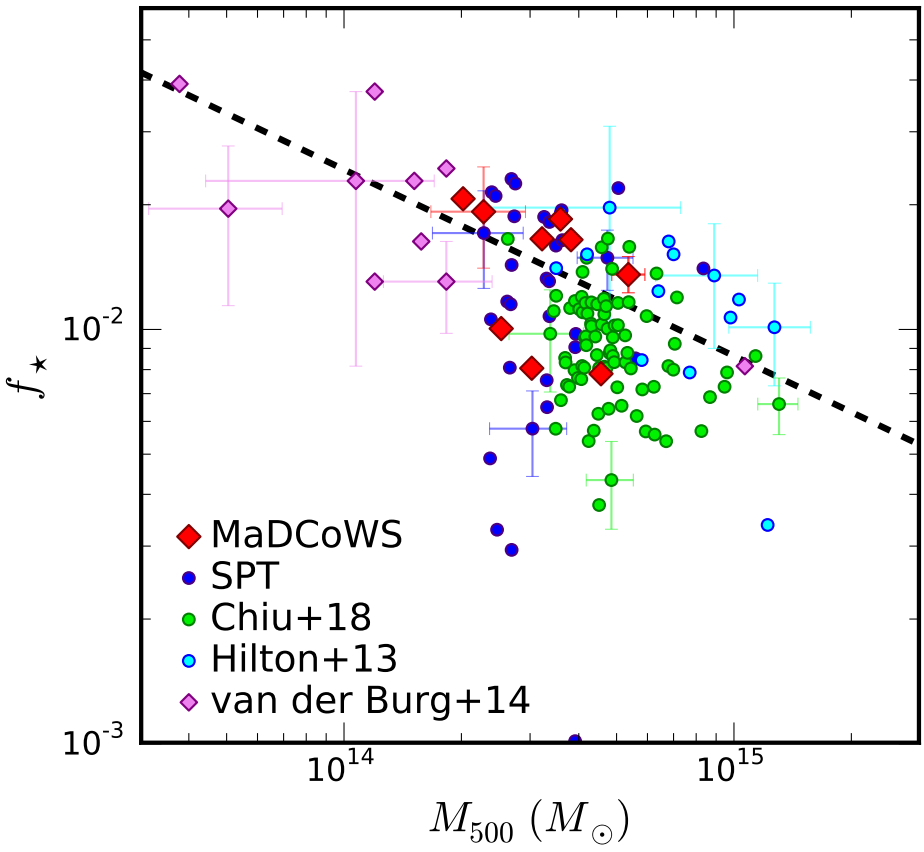

Figure 14 Comparison of the $f_\star$ measured in this work (red diamonds, blue circles) to $f_\star$ measured by Chiu et al. (2016, green circles), Hilton et al. (2013, cyan circles) and van der Burg et al. (2014, violet diamonds). All samples have been adjusted to be consistent with our methodology. Error bars are plotted for three representative clusters for each sample.

2.5.4 Systematics

There are three main sources of systematic error in our analysis. The largest is due to our background subtraction; this error is represented by the black error bars in Figure 17. We quantify the size of this uncertainty by measuring the background luminosity from the SDWFS field in $1'$ radius cutouts across the field and measure the scatter in this background to estimate small-scale variation due to clustering. We add this scatter in quadrature with the field-to-field scatter derived by comparing SDWFS to similar measurements in the EGS (Davis et al., 2007) and COSMOS fields (Scoville et al., 2007). Since this is an error in the luminosity—and therefore the stellar mass—of each cluster, the size of the systematic error in $f_\star$ decreases with increasing M_{500}. This systematic error is a uniform shift affecting both the MaDCoWS and SPT clusters equally, so it does not affect our comparison of the infrared and ICM selection methods.

The second source of systematic uncertainty in the absolute value of $f_\star$ for our clusters is our choice of stellar mass-to-light ratio. There are two components to this systematic. The first is the choice of tau model described in §2.4.1, but this is a small effect. The 1.6μm bump is largely insensitive to the star formation history of the galaxy, so varying tau does not have a large effect on the M/L ratio. The second component is the choice of IMF. We use a Chabrier (2003) IMF, but other choices, such as the Salpeter (1955) IMF, are also common. This has a large effect on our M/L ratio, almost doubling it for a 1 Gyr tau model. However, since this is easily corrected for and does not affect any comparisons we make, we do not include

it in our systematic error bar in Figure 17.

A final possible source of systematic uncertainty stems from our rejection of cluster non-members using magnitude cuts. Our choice of $m^* - 2$ as a brightness threshold strikes a balance between maximizing the bright members included and minimizing the inclusion of bright foreground interlopers. Although this choice is a somewhat arbitrary threshold, changing it has only a small effect on our values for $f_\star$ since we already statistically correct for non-member contamination, and one that is quite consistent from cluster-to-cluster. It does not make an appreciable difference to our analysis.

Our faint-end cutoff leads to a modest underestimate of the total stellar mass. Integrating a luminosity function with $\alpha = -0.8$ beyond $m^* + 1$ suggests we could be missing $\sim 25\%$ of the stellar mass from fainter galaxies. If we correct our stellar masses for this, the result is a simple multiplicative increase of all our $f_\star$ values, but by an amount less than both the scatter and the existing systematic error. Since this offset affects all clusters equally, it does not affect the scatter in either sample, or our comparison between the MaDCoWS and SPT stellar mass fractions. As a practical matter, the large uncertainties in α and m^* make it difficult to accurately quantify the size of this uncertainty, and thus we choose not to include it in our analysis.

2.6 Conclusions

We have measured the stellar mass fractions of twelve infrared-selected clusters from MaDCoWS and 33 SZ-selected clusters from the SPT-SZ survey and found little difference in average $f_\star$ between the two selection methods. We measured $f_\star$ using IRAC 3.6 μm images of the clusters at $z \sim 1$ as a proxy for stellar mass along with total masses derived from SZ measurements. We found that when accounting for mergers in the MaDCoWS sample and normalizing over the trend of stellar mass fraction with total mass, the infrared-selected MaDCoWS clusters have an average stellar mass fraction of $f_\star/G13 = 1.16 \pm 0.12$, higher than the average stellar mass fraction of $f_\star/G13 = 0.88 \pm 0.09$ for the SPT, but not significantly so.

We also compare our results to those of Hilton et al. (2013), van der Burg et al. (2014) and Chiu et al. (2016) who also looked at stellar mass fractions in cluster samples of comparable mass and redshift to ours. When we correct for the differences between our methodologies and those of the other studies, we find our results are consistent with all three and they support our result that infrared-selected clusters do not have an appreciably higher mean $f_\star$than SZ-selected clusters. We also compare the value we calculate for m^* of the IRAC 3.6 μm luminosity function to that found by Muzzin et al. (2008), Mancone et al. (2010) and Wylezalek et al. (2014) and find similar results.

We found an unexpectedly large range in the stellar mass fractions of individual clusters in the SPT sample and a larger range and scatter in $f_\star$ than in our MaDCoWS clusters. It is possible that the SZ-selected SPT clusters give a

fairer sample of the full range of $f_\star$ than the infrared-selected MaDCoWS clusters do. Future work with MaDCoWS will compare $f_{\rm gas}$ measurements in infrared- and SZ-selected cluster samples to look for a comparable selection effect in the latter.

Finally, we have presented SZ observations of seven new MaDCoWS clusters and new spectroscopic redshifts for five clusters. Among the SZ observations of the seven new MaDCoWS clusters is MOO J1521+0452, which at $z = 1.31$ is one of the most massive clusters yet found at $z \geq 1.3$. Along with the previous discovery of a cluster of $M_{500} = (5.36^{+0.55}_{-0.50}) \times 10^{14}\ M_\odot$ at $z = 1.19$, reported in Gonzalez et al. (2015), this further demonstrates the ability of MaDCoWS' nearly all-sky infrared selection to find the most massive clusters at high redshifts.

CHAPTER 3

THE MASSIVE AND DISTANT CLUSTERS OF WISE SURVEY XI: STELLAR MASS FRACTIONS AND LUMINOSITY FUNCTIONS OF MADCOWS CLUSTERS AT $Z \sim 1$

Submitted to ApJ as *Decker et al., 2022*

Abstract

We present stellar mass fractions and composite luminosity functions (LFs) for a sample of 12 clusters from the Massive and Distant Clusters of WISE Survey (MaDCoWS) at a redshift range of $0.951 \leq z \leq 1.43$. Using SED fitting of optical and deep mid-infrared photometry, we establish the membership of objects along the lines-of-sight to these clusters and calculate the stellar masses of member galaxies. This allows us to calculate the stellar mass of the clusters much more precisely than in previous works. We find stellar mass fractions for these clusters largely consistent with previous works, including appearing to display a negative correlation with total cluster mass. We measure a composite 3.6 μm LF down to $m^* + 2.5$ for all 12 clusters. Fitting a Schechter function to the LF, we find a characteristic 3.6 μm magnitude of $m^* = 19.83 \pm 0.12$ and faint-end slope of $\alpha = -0.81 \pm 0.10$ for the full sample at a mean redshift of $\bar{z} = 1.18$. We also divide the clusters into high- and low-redshift bins at $\bar{z} = 1.29$ and $\bar{z} = 1.06$ respectively and measure a composite LF for each bin. We see a small, but statistically significant evolution in m^*

and α—consistent with passive evolution—when we study the joint fit to the two parameters, which is probing the evolution of faint cluster galaxies at $z \sim 1$. This highlights the importance of deep IR data in studying the evolution of cluster galaxy populations at high-redshift.

3.1 Introduction

The evolution of galaxies in clusters both influences and is influenced by the partitioning of baryons between the stars in galaxies and the hot gas of the intracluster medium (ICM). The stellar mass fraction of a cluster—that is, the fraction of the total mass in stars—$f_\star$, offers an *in situ* measurement of this partitioning. Measuring $f_\star$ and its relation to other cluster properties can give insight into the feedback processes that drive the cycling of baryons between states and which affect how galaxies grow and evolve (e.g., Lin et al., 2003; Ettori et al., 2006; Conroy et al., 2007). In addition, the shape of the cluster luminosity function (LF) offers insight into the mass-assembly history of the cluster. The near-infrared (NIR) LF is a useful proxy for the stellar mass function, as the luminosity in those bands is tightly correlated with stellar mass. The NIR LF parameters and how they evolve over time therefore reflect the mass-assembly history of galaxies in the cluster (Kauffmann & Charlot, 1998).

Previous studies such as Gonzalez et al. (2013) have analyzed the trend of $f_\star$ with total cluster mass at $z \sim 0.1$ and found an anti-correlation. This suggests that in the local universe, larger clusters retain their gas better and are less efficient at

forming stars. In Decker et al. (2019), we also studied the trend of $f_\star$ with cluster mass for a sample of infrared-selected clusters at high redshift and compared this to a sample of ICM-selected clusters at comparable redshifts to look for differences due to selection. While we found a larger scatter in $f_\star$ in the ICM-selected clusters, there was no significant offset between the two samples. We also measured a relationship between $f_\star$ and total mass that was consistent with that found by Gonzalez et al. (2013), but the scatter and systematic uncertainties were too high to draw firm conclusions.

Cluster LFs follow a Schechter distribution (Schechter, 1976) of the form

$$\Phi(m) = \frac{\ln(10)}{2.5}\Phi^* 10^{-0.4(m-m^*)(\alpha+1)}\exp(-10^{-0.4(m-m^*)})$$

where the overall scaling is paramaterized as Φ^*, the characteristic magnitude 'knee' at the bright end is parameterized as m^* and the slope of the faint-end of the function is parameterized as α. Many studies have examined the rest-frame NIR LF of galaxy clusters (e.g., de Propris et al., 1999; Strazzullo et al., 2006; Muzzin et al., 2007; Mancone et al., 2012; Wylezalek et al., 2014; Chan et al., 2019) to measure the characteristic magnitude of the cluster LF at different redshifts. However, measuring m^* becomes more difficult at high-redshift because there is a strong degeneracy between m^* and α. Therefore meaningfully measuring the former at high-redshift requires increasingly deep mid-infrared data to also constrain the latter. Indeed, few previous studies have measured the NIR LF for all cluster members (i.e., those both on and off the red-sequence) at $z > 1$ down to a depth sufficient to jointly fit both m^* and α.

To address these problems, we measure stellar mass fractions and LFs for a sample of clusters from the Massive and Distant Clusters of *WISE* Survey (MaDCoWS, Gonzalez et al., 2019). For this work we use MaDCoWS clusters with previously measured Sunyaev-Zel'dovich (SZ, Sunyaev & Zeldovich, 1970, 1972) masses, which allows us to measure $f_\star$ and compare to the total mass. We also limit our sample to clusters that have deep mid-infrared photometry. This allows us to determine the stellar mass more robustly than in our previous study, Decker et al. (2019), and also allows us to measure the rest-frame NIR LF down to sufficiently faint magnitudes to fit m^* and α jointly. Finally, we limit our sample to clusters that—in addition to the above criteria—also have optical follow-up data. This allows us to better determine which objects are true members of the clusters, reducing systematic errors in our measurements both of $f_\star$ and the LF parameters.

We present our cluster sample and describe in more detail the follow-up data in §3.2 and describe our analysis in §3.3. Our results for both $f_\star$ and the LFs are in §3.4 and we discuss those results in §3.5. Throughout this paper we use AB magnitudes in all bands and a concordance ΛCDM cosmology of $\Omega_m = 0.3$, $\Omega_\Lambda = 0.7$ and $H_0 = 70$ km s^{-1} Mpc^{-1}. We define r_{500} as the radius inside which the cluster density is 500 times the critical density of the universe at the cluster redshift and M_{500} as the mass interior to that radius.

3.2 Cluster Sample and Data

For this work, we use 12 clusters from the MaDCoWS catalog. These clusters are drawn from the much larger sample with SZ masses from Brodwin et al. (2015), Gonzalez et al. (2015), Decker et al. (2019), Di Mascolo et al. (2020), Dicker et al. (2020), and Orlowski-Scherer et al. (2021) and the SZ masses from different facilities are generally in good agreement with each other. This sample of clusters are selected to have previously reported spectroscopic redshifts, deep follow-up imaging in the mid-infrared, and optical follow-up photometry. This arrangement of follow-up data was chosen as it allows us to constrain the membership of clusters using photometric redshift fitting; it includes eight of the 12 clusters from Decker et al. (2019). The clusters are listed in Table 4, along with their redshifts and information about the relevant observations. Details of the follow-up data are given below and details of the SZ observations and mass calculations can be found in the relevant papers.

3.2.1 Optical Data

All 12 clusters have r- and z-band imaging from the Gemini Multi-Object Spectrograph (GMOS, Hook et al., 2004) on the Gemini Telescopes in Hawai'i and Chile. These images were taken in several programs: GN-2013A-Q-44, GN-2013B-Q-8 (both PI: Brodwin), GN-2015A-Q-42 (PI: Perlmutter), GN-2015A-Q-4 (PI: Stalder), GN-2017B-LP-15, GN-2018A-LP-15 (both PI: Stanford), and GS-2019A-FT-205 (PI: Decker). There was a heterogenous mix of observing strategies for these

programs, partly due to the different sensitivities of the GMOS CCD during different observing cycles. However they result in a comparable depth for all the clusters. All of the exposure times are listed in Table 4.

3.2.2 Infrared Data

These clusters have mid-infrared data from the 3.6 μm and 4.5 μm bands of the *Spitzer Space Telescope* Infrared Array Camera (IRAC, Fazio et al., 2004). They were imaged in programs 12101 and 13214 (both PI: Brodwin) and the exposure times for each cluster and each band are listed in Table 4. Both programs had the same observing strategy, with the varying exposure times designed to detect galaxies to a relatively uniform depth relative to m^* in different IR background regions.

3.2.3 Catalogs

For each cluster, we used the optical and infrared imaging described in §3.2.1 and §3.2.2 to make four-band (r, z, 3.6 μm, 4.5 μm) photometric catalogs. For each cluster, all four images were transformed onto the same image scale using SWarp (Bertin et al., 2002). The catalogs were produced by running Source Extractor (SE, Bertin & Arnouts, 1996) in dual-image mode on all four SWarped images, using the 3.6 μm image as the detection image. The SE parameters were the same as in Decker et al. (2019). The final catalogs used 2″ diameter aperture photometry in the optical bands and 4″ diameter corrected to 24″ diameter aperture photometry in the infrared bands. The correction from 4″ to 24″ used the IRAC aperture corrections given in Ashby et al. (2009).

Table 4. Summary of observations of MaDCoWS clusters used in this analysis

Cluster ID	RA (J2000)	Dec. (J2000)	z	$t_{\rm exp}$ (s) r-band	$t_{\rm exp}$ (s) z-band	$t_{\rm exp}$ (s) 3.6 μm	$t_{\rm exp}$ (s) 4.5 μm	SZ Facility
MOO J0105+1323	01:05:31.5	+13:23:55	1.143	13×120	9×150	14×100	33×100	CARMA[a]
MOO J0319−0025	03:19:24.4	−00:25:21	1.194	5×180	12×80	10×100	24×100	CARMA[b]
MOO J0917−0700	09:17:04.7	−07:00:08	1.10	6×180	6×60	10×100	24×100	ALMA[c]
MOO J1111+1503	11:11:42.6	+15:03:44	1.32	4×300	16×80	14×100	33×100	CARMA[a]
MOO J1139−1706	11:39:28.2	−17:06:31	1.31	12×120	10×60	14×100	34×100	ALMA[c]
MOO J1142+1527	11:42:45.1	+15:27:05	1.189	5×180	12×80	14×100	33×100	CARMA[d]
MOO J1155+3901	11:55:45.6	+39:01:15	1.009	5×180	12×80	12×100	26×100	CARMA[b]
MOO J1329+5647	13:29:50.7	+56:48:03	1.43	6×180	6×60	10×100	24×100	GBT[e]
MOO J1506+5136	15:06:22.7	+51:36:45	1.09	35×120	8×60	10×100	24×100	GBT[e]
MOO J1514+1346	15:14:42.7	+13:46:31	1.059	5×180	12×80	10×100	24×100	CARMA[b]
MOO J1521+0452	15:21:04.6	+04:52:08	1.312	12×120	9×150	12×100	26×100	CARMA[a]
MOO J2206+0906	22:06:28.6	+09:06:32	0.951	5×180	12×80	10×100	24×100	CARMA[a]

[a]Decker et al. (2019)

[b]Brodwin et al. (2015), with mass recalculated in Decker et al. (2019)

[c]Di Mascolo et al. (2020)

[d]Gonzalez et al. (2015), with mass recalculated in Decker et al. (2019)

[e]Dicker et al. (2020)

For comparison and validation of our fitting (see next section) we also made a field catalog using r- and z- band images from the Cosmic Evolution Survey (COSMOS, Scoville et al., 2007) and 3.6 μm and 4.5 μm images from the *Spitzer* Extended Deep Survey (Ashby et al., 2013) in the footprint where those two surveys overlap. These catalogs were made with the same procedure as our cluster catalogs. Because the *Spitzer* Extended Deep Survey imaging is deeper than our IRAC imaging, we artificially degraded the field catalog data in the IRAC bands to match our cluster catalogs. We do this by adding a small additional scatter to the measured fluxes. This scatter is randomly drawn from a Gaussian distribution with a width equal to the quadrature difference of the (higher) error in our photometry and the error in the Extended Deep Survey.

3.3 Analysis

3.3.1 Cluster Membership

We used EAZY (Brammer et al., 2008) to fit spectral energy distributions (SEDs) to the four-band photometry for each object in our cluster catalogs and our field catalog. The result was a best-value and a probability density function (PDF) of the redshift for each object. We compared the best-value fitted redshifts in the field catalog to the multi-band photometric redshifts from the COSMOS catalog (Laigle et al., 2016) to determine the error in our photometric redshift fitting. After running an iterative 3σ clipping routine, we found an error in our photometric redshifts of $\sigma_z = 0.17(1+z)$. This error is relatively high, due to the small number of photometric

bands, but is sufficient to isolate cluster members with a low interloper rate.

To determine which objects in the cluster catalogs were consistent with being members of the cluster, we used the full PDFs output by EAZY. For each object, we first smoothed the output PDF with a Gaussian corresponding to the $\sigma_z = 0.17(1+z)$ scatter in our redshift fitting. We then integrated under this convolved PDF in the range $z_{cl} - \sigma_z \leq z < z_{cl} + \sigma_z$, as shown in Figure 15. If this integrated probability was above 0.3, we considered the object to be a cluster member; everything else was removed from the catalog. We chose 0.3 as a cutoff to maximize completeness while still removing the bulk of the line-of-sight interlopers. Because our cluster masses were only measured out to r_{500}, we also removed from our cluster catalogs objects lying at a projected distance more than that distance from the cluster center. Since this method would still not remove every line-of-sight interloper, we also ran this analysis on the field catalog at each cluster redshift. This provided a set of 12 field catalogs, each containing the objects from the full field catalog that our analysis would consider being consistent with cluster members. These 'interloper' catalogs provided us a baseline that allowed us to statistically remove line-of-sight interlopers from our analysis.

3.3.2 Completeness

We measured the photometric completeness of our cluster catalogs by randomly placing artificial sources into our detection images, running SE, and recording how many of these artificial sources were detected by SE. For each cluster we placed a

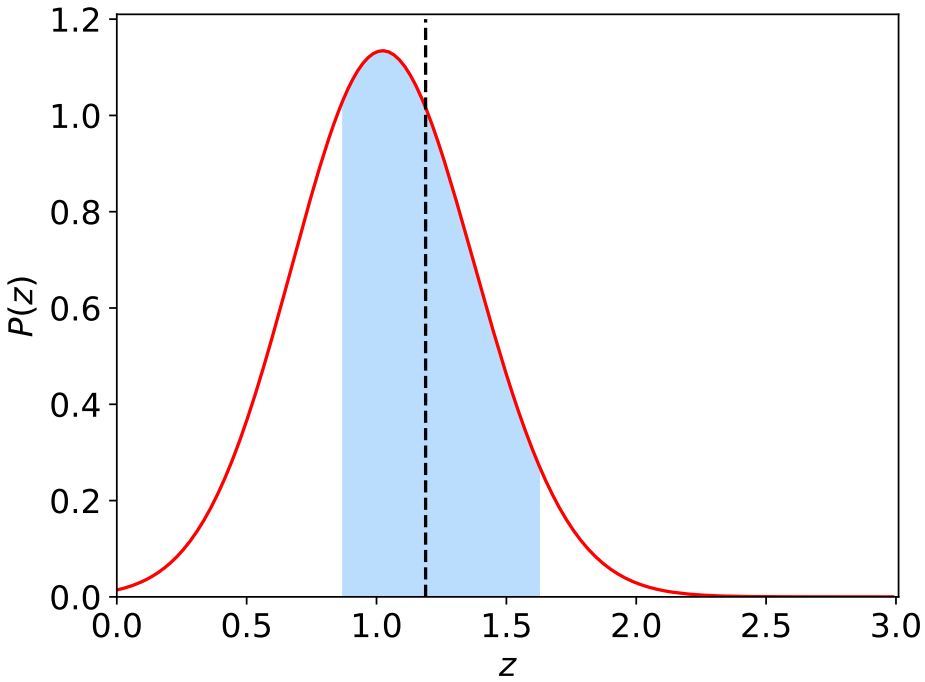

Figure 15 Smoothed output PDF from EAZY of a spectroscopically-confirmed (from Gonzalez et al., 2015) member of MOO J1142+1527. The cluster redshift of $z = 1.19$ is denoted by the black dashed line and the shaded blue region is the integration range around the cluster redshift. The integrated probability in that region is 0.65, well above our membership threshold.

total of one thousand sources per quarter-magnitude bin in batches of ten sources each. The average 3.6 μm completeness curve of the sample is shown as a light blue line in Figure 16. The completeness reaches a plateau at around 95% at the bright end because of the high density of infrared sources in the clusters. The vertical dashed line represents the average 5σ limit of our data in that cluster. The errors on the completeness in each bin are Poisson errors and are approximately 3% per bin.

In addition to measuring the photometric completeness of our catalogs, we also measured the completeness of our cluster member selection algorithm. Each object in the field catalogs has a redshift from COSMOS, and some coincidentally lie at the redshifts of our clusters. For each cluster, we isolated these objects from the field catalog and ran our membership selection algorithm on them. As with the detection completeness, we split the objects into quarter-magnitude bins in 3.6 μm. For each quarter-magnitude bin, we define the membership completeness as the fraction of objects that our algorithm correctly identified as lying at the cluster redshift. Since unlike with the artificial sources we used for our detection completeness, there were a variable number of objects in each bin, we calculated the error on the membership completeness using bootstrap resampling. The average membership completeness is shown in Figure 16 as a dark blue line. Since there were not enough objects at the bright end to have meaningful statistics, we fixed the completeness in that region to unity.

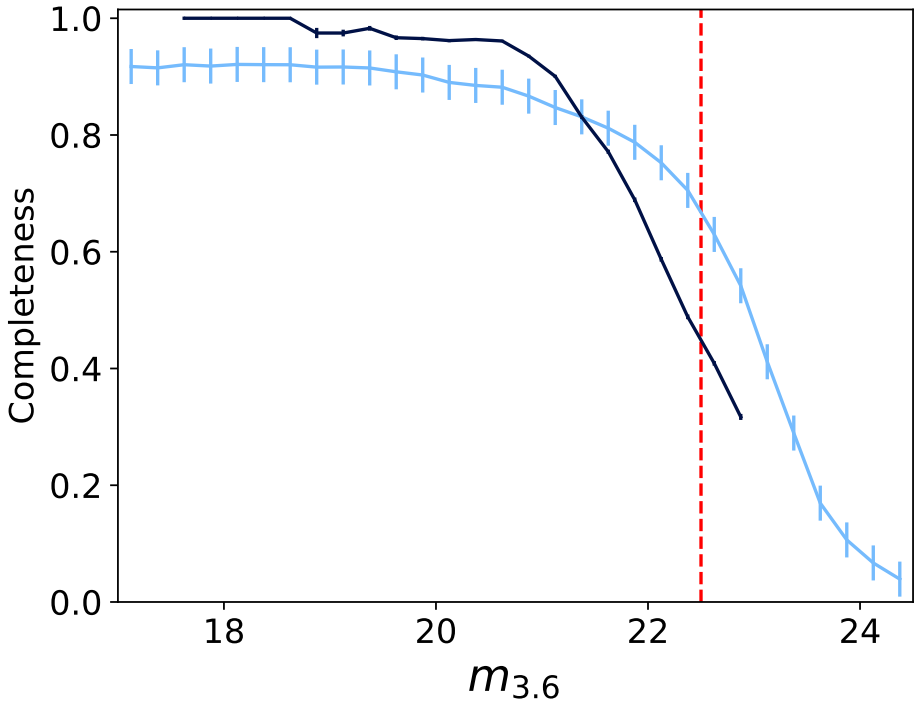

Figure 16 Mean detection (light blue) and membership (dark blue) completeness for the clusters in our sample. The error bars on the detection completeness are Poisson errors and the error bars on the membership completeness are from bootstrap re-sampling. At the bright end of the membership completeness curve (3.6 μm$<$ 18.75) there were not enough field objects to produce meaningful statistics, so we fixed the completeness to unity. The vertical dashed red line at the faint end represents the average 5σ detection limit.

3.3.3 Stellar Mass

We used another SED-fitting program, FAST (Kriek et al., 2009), on the cluster catalogs to calculate the stellar masses of the objects along the line of sight to the cluster. For this, we adopted a Bruzual & Charlot (2003) model, a Chabrier (2003) initial mass function, a solar metallicity, and we fixed the redshift of each object in the catalog to the cluster redshift. We only fit to intrinsic properties of the galaxies, in particular stellar mass. As with the redshift fitting, we also ran FAST on the field catalog to calibrate the errors in our fitting and to establish how much field contribution to expect even after removing interlopers. Comparing the stellar masses we measured in this way to the stellar masses given in the COSMOS catalog, we adopted a uniform 0.2 dex uncertainty in our stellar mass measurements.

With this final catalog of objects identified as being at the cluster redshift by EAZY, lying within a projected distance of r_{500} from the cluster center, and with stellar masses measured from FAST, we calculated the total stellar mass of the clusters inside r_{500}. For each cluster, we first scaled the stellar mass of each object by the photometric and membership completeness corrections in §3.3.2. We then summed these scaled masses to get a total line-of-sight stellar mass for the cluster. Since this is still expected to include some small number of interlopers, we measured the total stellar mass of the statistical interloper catalog in the same way. We scaled that mass to the area of the cluster catalog and subtracted this expected interloper contribution—approximately 10% of the line-of-sight mass for most of the clusters—from the line-of-sight mass to get the total cluster stellar mass. We calculated the

error on the stellar mass of each cluster by propagating the error of the stellar mass of each individual object in the cluster and field catalogs, measured in §3.3.1.

3.3.4 Luminosity Function

We used our membership selection and deep IRAC photometry to produce composite 3.6 μm LFs for our cluster sample. For each cluster, we first evolution-corrected the 3.6 μm apparent magnitudes of both the cluster and interloper catalog to the mean redshift of the sample using EZGal (Mancone & Gonzalez, 2012) and assuming passive evolution after an initial starburst at $z_f = 3.0$. We removed the brightest cluster galaxy (BCG) from the cluster catalog and then binned these evolution-corrected catalogs into quarter-magnitude bins to produce a line-of-sight LF and a background LF for each cluster. We then applied both the completeness corrections described in §3.3.2 as a function of magnitude to both LFs. Finally, we scaled the background LF to match the surface area of the cluster and subtracted it off the line-of-sight LF to produce the individual cluster LF. These individual LFs were stacked to form the composite LF for the sample. The error on each value in the individual LFs is from adding in quadrature the Poisson errors of both the line-of-sight and interloper LFs and the errors on both completeness corrections. The error on each value in the composite LF is the quadrature sum of those errors from the individual LFs.

3.4 Results

3.4.1 Stellar Mass Fractions

The stellar mass fractions we measure for these clusters are given in Table 5 and Figure 17 shows $f_\star$ versus M_{500} for the 12 clusters of this work, plotted as red diamonds, where filled diamonds denote clusters also in Decker et al. (2019). For comparison, we also plot the low-redshift trend line measured by Gonzalez et al. (2013) as a green dashed line. Clusters that were also studied in Decker et al. (2019) are indicated in Table 5.

Figure 18 shows the direct comparison of $f_\star$ for the eight clusters common to both this work and Decker et al. (2019). With only one exception, MOO J0105+1323, the $f_\star$ we measure in this work is higher than the $f_\star$ we found in Decker et al. (2019) and for no clusters is it significantly lower. This is expected as in both works we use IRAC 3.6 μm to measure $f_\star$—either directly or indirectly—and the much deeper 3.6 μm data in this work allow us to include stellar mass from galaxies that were too faint to be detected in our previous work. Using 3.6 μm luminosity as a proxy for stellar mass, we quantify the amount of 'extra' stellar mass to which we are sensitive with these deeper data by integrating down the composite LF we measure in §3.4.2. Integrating down to the depth of our current data versus integrating to the depth of our data in Decker et al. (2019) shows we are sensitive to approximately 25% more stellar mass with these deep IRAC data than we were previously. This is consistent with the change in $f_\star$ we see in all but two of the clusters. Note that this does not necessarily mean that each cluster *has* a 25% increase in stellar

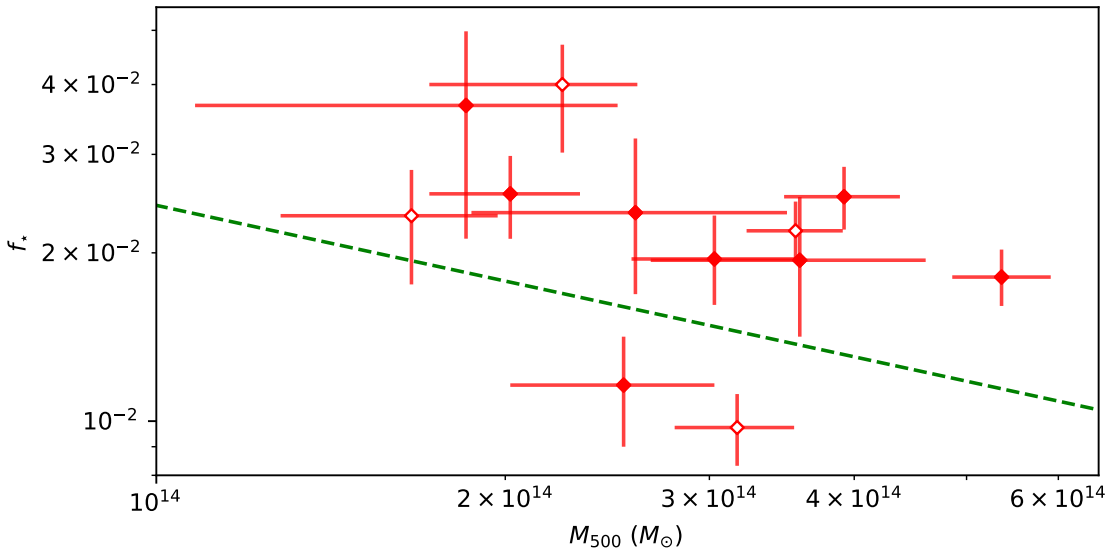

Figure 17 Stellar mass fraction versus total mass for the MaDCoWS clusters in this analysis, plotted as filled red diamonds for clusters in Decker et al. (2019) and open diamonds otherwise. The error on $f_\star$ is from adding the percent stellar mass error from §3.3.3 and the percent error of the total mass of the cluster in quadrature. The green dashed line is the low-redshift relation from Gonzalez et al. (2013), plotted to provide continuity with Decker et al. (2019). Note that the systematic uncertainty errors from Decker et al. (2019) are no longer plotted, as the systematic uncertainties from our previous study are now incorporated into the statistical uncertainty, or shrunk to the level of inconsequence.

Table 5. MaDCoWS Stellar Mass Fractions

ID	M_{500} ($10^{14}\ M_\odot$)	$M_\star$ ($10^{12}\ M_\odot$)	$f_\star$ (10^{-2})
MOO J0105+1323*	$3.92^{+0.46}_{-0.44}$	10.6 ± 0.58	$2.70^{+0.35}_{-0.34}$
MOO J0319−0025*	$3.03^{+0.54}_{-0.46}$	6.32 ± 0.49	$2.09^{+0.40}_{-0.36}$
MOO J0917−0700	$1.66^{+0.31}_{-0.38}$	4.08 ± 0.36	$2.48^{+0.51}_{-0.61}$
MOO J1111+1503*	$2.02^{+0.30}_{-0.30}$	4.95 ± 0.40	$2.45^{+0.42}_{-0.42}$
MOO J1139−1706	$2.24^{+0.36}_{-0.52}$	8.40 ± 0.66	$3.80^{+0.68}_{-0.93}$
MOO J1142+1527*	$5.36^{+0.55}_{-0.50}$	9.91 ± 0.59	$1.85^{+0.22}_{-0.20}$
MOO J1155+3901*	$2.53^{+0.50}_{-0.51}$	3.21 ± 0.29	$1.27^{+0.28}_{-0.28}$
MOO J1329+5647	$3.56^{+0.35}_{-0.33}$	7.89 ± 0.64	$2.25^{+0.28}_{-0.27}$
MOO J1506+5136	$3.17^{+0.38}_{-0.37}$	3.59 ± 0.27	$1.16^{+0.16}_{-0.16}$
MOO J1514+1346*	$2.39^{+0.51}_{-0.83}$	7.34 ± 0.49	$3.97^{+1.42}_{-1.67}$
MOO J1521+0452*	$3.59^{+1.02}_{-0.92}$	7.15 ± 0.60	$1.99^{+0.59}_{-0.54}$
MOO J2206+0906*	$2.95^{+0.82}_{-0.68}$	6.52 ± 0.40	$2.52^{+0.90}_{-0.72}$

*Also in Decker et al. (2019)

mass, but that our improved depth allows us to robustly measure the stellar mass that much further down the LF. All things being equal this will lead to an increase in the measured stellar mass, but we also improve our rejection of non-members and our measurement of the stellar mass of individual objects, both of which may reduce the stellar mass relative to Decker et al. (2019). Taken together, these effects mean that we should not be surprised to see an increase in stellar mass of *up to* 25%, but the increase in mass for each cluster will vary. All of the measurements are *significantly* more precise than they were in Decker et al. (2019); not only are the measurements deeper and more accurate, they also no longer come with the large systematic uncertainty that the measurements in Decker et al. (2019) had. The remaining errors in $f_\star$ are driven primarily by the large uncertainties in the total cluster mass. Integrating the analytic, fitted LF shows this analysis is sensitive to $\geq 95\%$ of the stellar mass in each cluster.

MOO J0319−0025 and MOO J1142+1527 exhibit larger jumps in $f_\star$ than the 25% we expect simply from the deeper data. Those increases likely come from the improved way we are determining both cluster membership and stellar mass. Using a fuller sampling of the galaxy SEDs—even in just four bands—gives us a better and more consistent measurement of the stellar mass of each object versus what we were able to do in Decker et al. (2019).

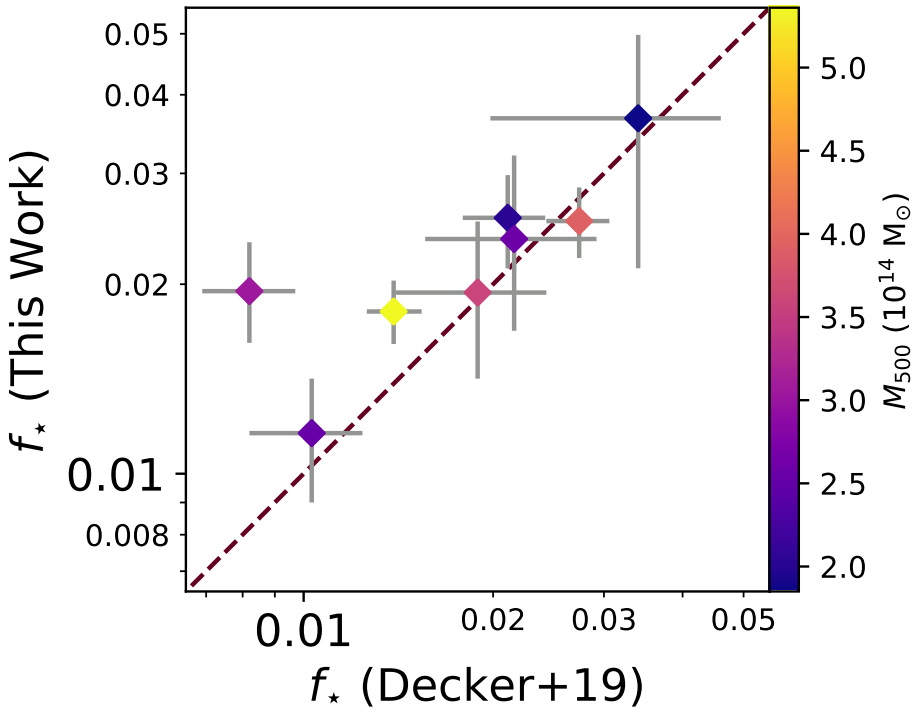

Figure 18 Comparison of the stellar mass fractions of clusters common to this work and to Decker et al. (2019). The dashed red line represents where the old and new mass fractions would be equal. Clusters falling above the line have a higher $f_\star$ in this work and clusters falling below the line have a higher $f_\star$ in Decker et al. (2019). The color of each point corresponds to the mass of the cluster.

Table 6. MaDCoWS Sample Data and Schechter Parameters

Sample	N_{cl}	$\bar{z}$	$\bar{M_{500}}$ ($10^{14} M_\odot$)	m^*	α	ϕ^* (dN dm^{-1} cluster^{-1})
All	12	1.18	2.96	19.83 ± 0.12	-0.81 ± 0.10	98 ± 13
High-z	6	1.29	3.30	19.86 ± 0.20	-0.95 ± 0.15	89 ± 20
Low-z	6	1.06	2.62	19.69 ± 0.22	-0.77 ± 0.16	96 ± 20

3.4.2 Luminosity Functions

The composite LF for our full sample of 12 clusters is shown in Figure 19. We fit a parameterized Schechter function to the measured LF using a Monte Carlo Markov Chain (MCMC) running a Metropolis-Hastings algorithm. The best-fit Schechter function is shown as a dashed line in the figure, with the lighter region showing the 1σ error on the best fit. The best fit parameters and the error on them are derived from the mean and standard deviation of the MCMC posterior chains after discarding the initial 'burn-in' period. These values are listed in Table 6 along with the mean redshift and mass of the sample.

Because m^* and α are covariant, in addition to the simple errors given in Table 6, we also plot the 1σ (dark) and 2σ (light) covariance ellipses for m^* and α for the full sample in Figure 20. This shows the extent of the degeneracy between m^* and α as well as the axis along which our uncertainty is concentrated.

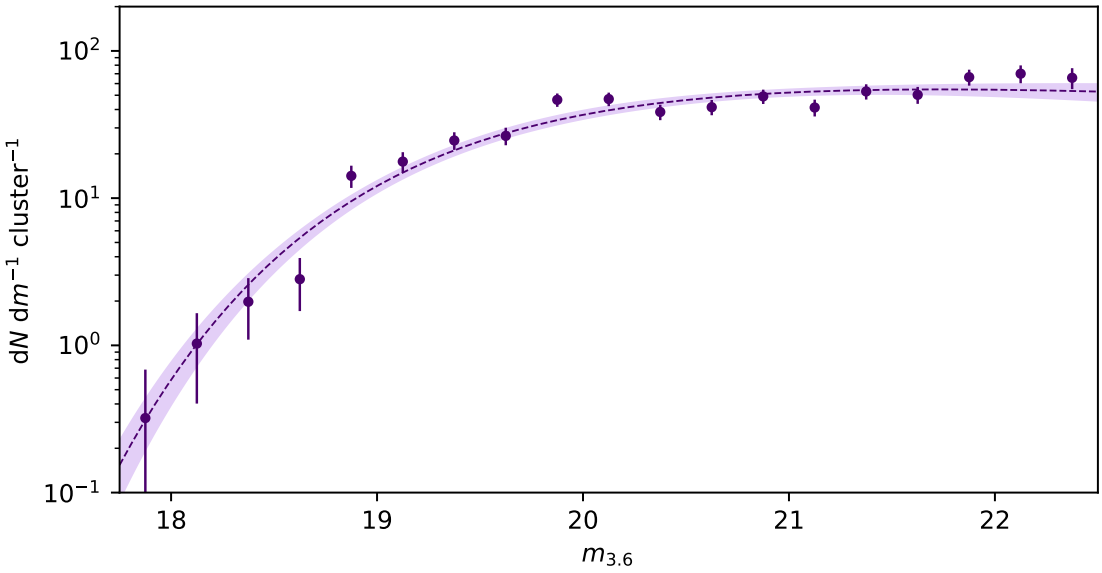

Figure 19 Composite LF for the full sample of 12 clusters used in this analysis. The purple points are the average number of objects per magnitude per cluster in each quarter-magnitude bin and the error bars are derived from the Poisson error of the individual LFs and the completeness errors. The mean sample mass and redshift are given, as well as the best fits to the parameterized Schechter function and their errors, in Table 6. The best-fit Schechter function itself is shown as a dashed line and the shaded area represents the 1σ error on the best fit.

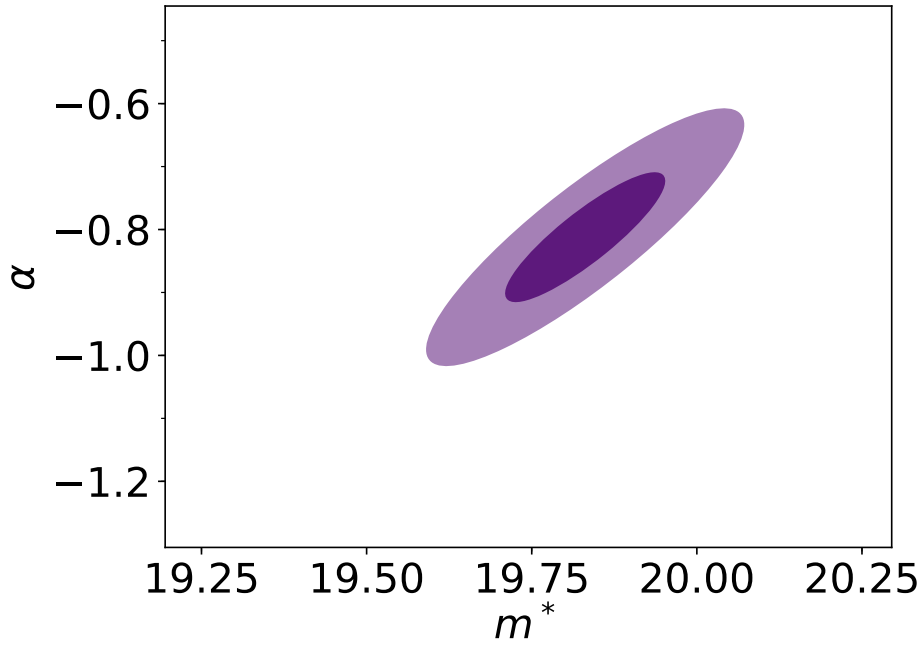

Figure 20 Covariance ellipses showing the 1σ (dark) and 2σ (light) errors and covariances in m^* and α for the average LF of all 12 clusters in this work.

Our sample is large enough that we also split our clusters into high- and low-redshift samples—splitting them at the median redshift of our sample, $z = 1.17$—and measure composite LFs for both of those. The measurement and fitting for these sub-samples is the same as for the full sample and the mean masses and redshifts for both sub-samples are also shown in Table 6, along with the best-fit Schechter function parameters to each LF. These LFs are shown in Figure 21. As with the full sample, we also plot the covariance between m^* and α for these two sub-samples in Figure 22. This figure shows that although the error bars for the individual parameters overlap between the two samples, there is a significant evolution from $z = 1.29$ to $z = 1.06$ in the LF as a whole. As discussed in §3.5.2.3, this is consistent with being driven by passive evolution in our sample. For comparison, we also plot in Figure 22 the outlines of the ellipses for the full sample from Figure 20.

We also explore fitting a sum of two Schechter function to our LFs, in a manner similar to Lan et al. (2016). This is motivated particularly by our high-redshift LF which seems to show an upturn at the faint end that is possibly more consistent with a second 'faint' Schechter function wit a steep faint-end slope. Although we can't rule out there being an upturn at the faint-end of our LFs, to the depth of our data ($\sim m^* + 2.5$) we find that this sum of Schechter functions is at best only a marginally better fit to the data, at a level that is well short of statistical significance.

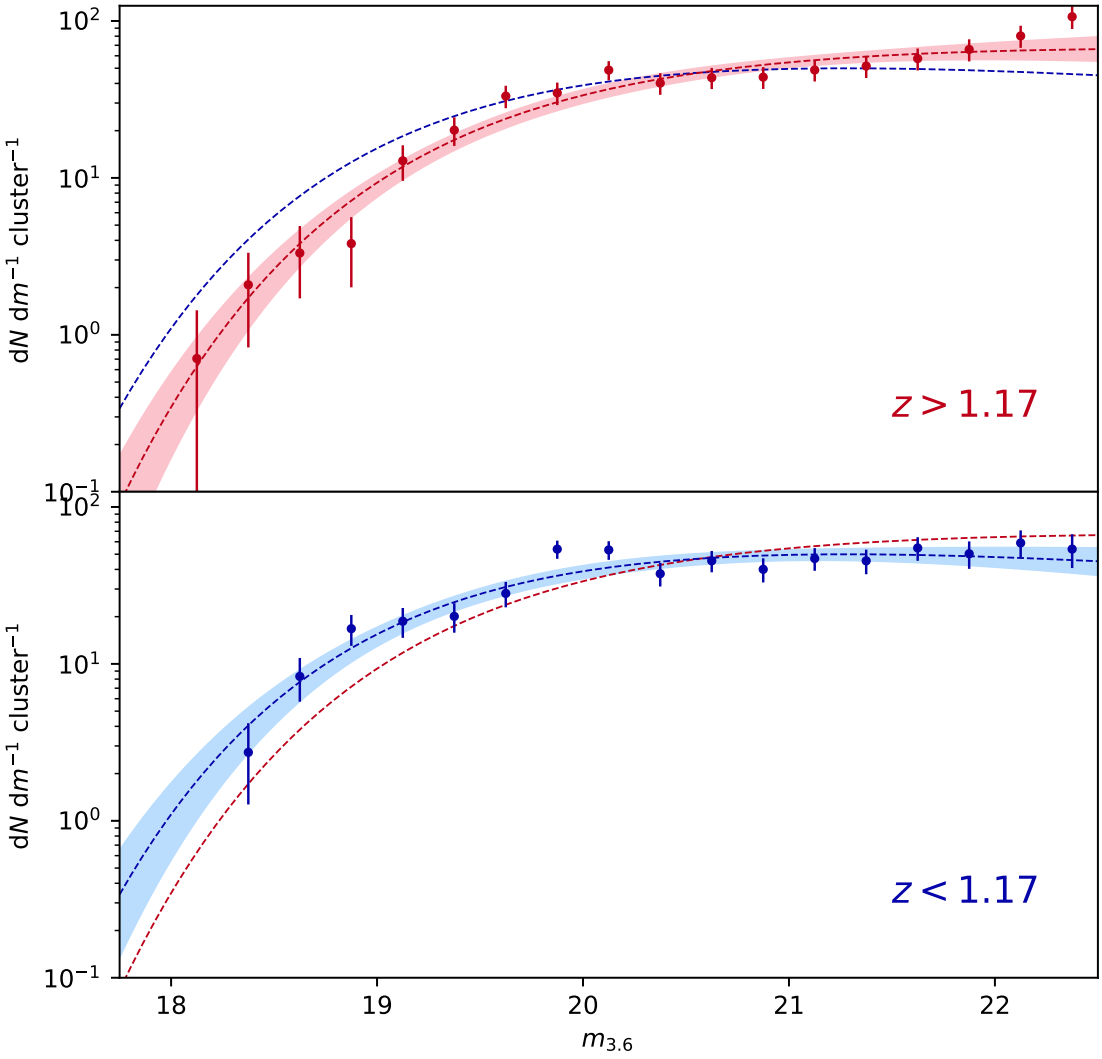

Figure 21 LFs for the high-redshift (upper, red) and low-redshift (lower, blue) subsamples. The best-fit Schechter functions are plotted as dashed lines with the 1σ error on the best fit shown as shaded regions. Each panel also shows the best fit line from the other panel as a dashed line of the relevant color.

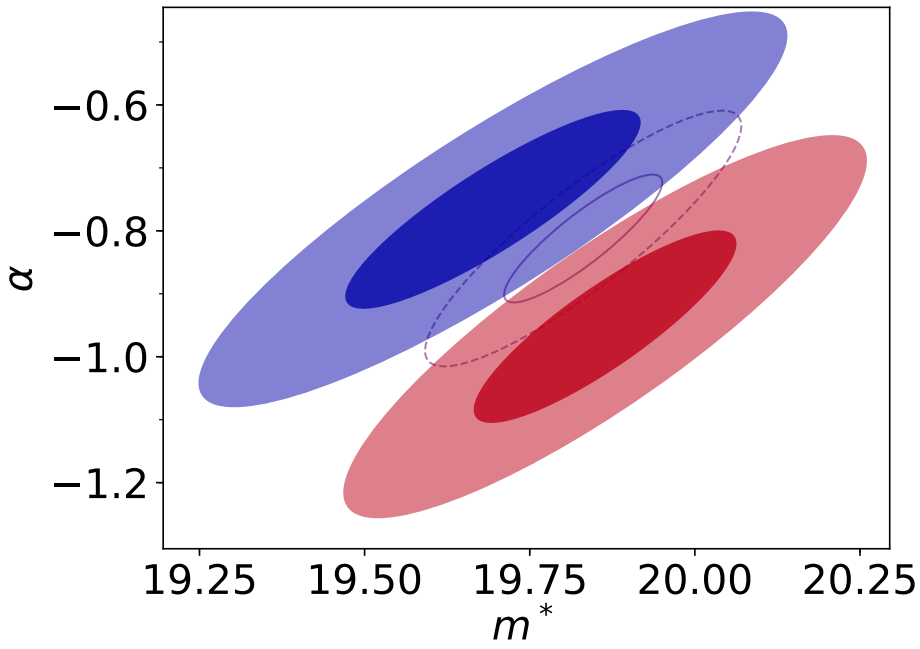

Figure 22 Covariance ellipses showing the 1σ (dark) and 2σ (light) errors and covariances in m^* and α for the high-redshift (red) and low-redshift (blue) sub-samples. For comparison, the whole-sample covariances ellipses from Figure 20 are outlined underneath.

3.5 Discussion

3.5.1 Stellar Mass Fraction

The stellar mass fractions we compute in this work display many of the same traits as the stellar mass fractions we calculated in Decker et al. (2019). The main difference is that the improved measurement of $f_\star$ has resulted in higher values overall, and ten of the twelve now lie slightly above the Gonzalez et al. (2013) line, nine of them significantly so.

Any departure from the Gonzalez et al. (2013) relation in this work would be interesting. Assuming a constant baryon fraction, the slope of the relation indicates how efficiently clusters of different mass are at converting gas into stars. Finding the same decreasing trend with total mass could indicate that there are mass-dependent processes slowing down or shutting off star formation at high-redshift as well as the local universe. However, as found in Giodini et al. (2009) and noted in Gonzalez et al. (2013), the assumption of a constant baryon fraction may not be a valid, especially at low cluster masses where active feedback can remove baryons from the cluster. Removing gas from lower mass clusters would also cause a decreasing trend of stellar mass fraction with total mass. If the stellar mass fractions we see here are indeed higher than those of low-redshift clusters, it would imply that there is an evolution in the total fraction of stars between $z \sim 1$ and the local universe.

But drawing any such conclusions from these data would be premature. Despite our improved measurements significantly reducing the stellar mass errors and removing the systematic errors on our measurements of $f_\star$, the remaining statistical

errors driven by the total mass error are still high enough that we cannot draw any significant conclusions about either the slope of the trend or its normalization. Figure 23 shows the best fit and error on the best fit trend line to our data. The slope of the Gonzalez et al. (2013) trend line is consistent with our measurements, but so is a flat trend line, with no relationship between $f_\star$ and M_{500}.

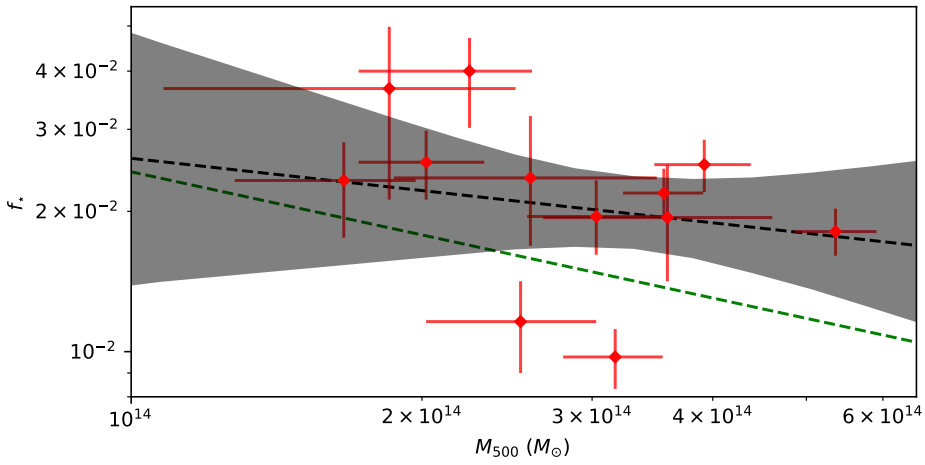

Figure 23 Plot of stellar mass fraction versus total mass with the best-fit trend line now plotted as a black dashed line, and the error on the fit shown as a dark shaded region. The scatter and the error in stellar mass fraction is large enough that the slope of the fit is consistent both with that of the Gonzalez et al. (2013) line and with a flat slope.

We showed in Decker et al. (2019) that outliers in $f_\star$ can indicate a cluster in a dynamical state that makes it hard to measure the total mass of the cluster. It is possible that the two low outliers in Figure 23 are unfairly driving some of the uncertainty in our fit. Removing them and fitting to the remaining clusters as shown in Figure 24 increases the best-fit slope, but the error and scatter are still

too high too draw any conclusions.

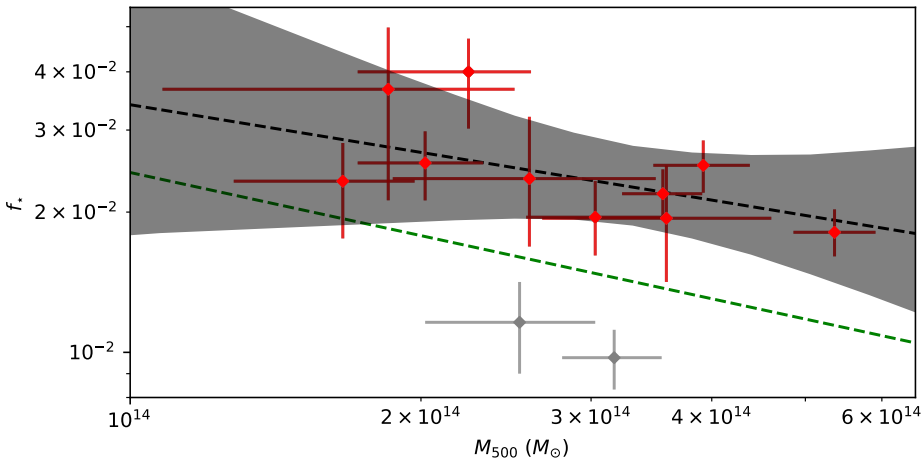

Figure 24 Plot of stellar mass fraction versus total mass with the the two outliers now plotted in grey and excluded from the fit. The resulting trend line is stepper than in Figure 23, but the shaded error region is still consistent with both a flat slope and the Gonzalez et al. (2013) trend line.

As discussed previously, much of this is due to the high error on the total mass of some of the clusters, which factors into the error on $f_\star$. For the well-measured clusters like MOO J1142+1527 on the right side of Figure 17, the $f_\star$ error is very small. Deeper SZ imaging on the MaDCoWS clusters is likely necessary to provide a significant measurement of properties related to the total mass.

3.5.2 Comparison to Other LF Studies

A comparison of our measurements of m^* and α to other works across a range of redshifts is shown in Figures 25 and 26. To facilitate comparison with some other studies, we again use EZGal to convert our apparent 3.6 μm magnitudes to absolute

H-band magnitudes. We use a Bruzual & Charlot (2003) model with a formation redshift of $z_f = 3.0$, a Chabrier (2003) initial mass function, and a solar metallicity to calculate the k-correction, but because we are already probing the rest-frame H-band with our 3.6 μm observations, the k-correction is almost entirely model-independent and changing the model parameters does not affect the k-correction by more than 0.01 at any of our redshifts. Doing this, we find $M^*_H = -23.91 \pm 0.12$ for our overall LF and $M^*_H = -24.09 \pm 0.20$ and $M^*_H = -23.80 \pm 0.22$ for the high- and low-redshift LFs, respectively. Figure 25 shows this comparison for M^*_H.

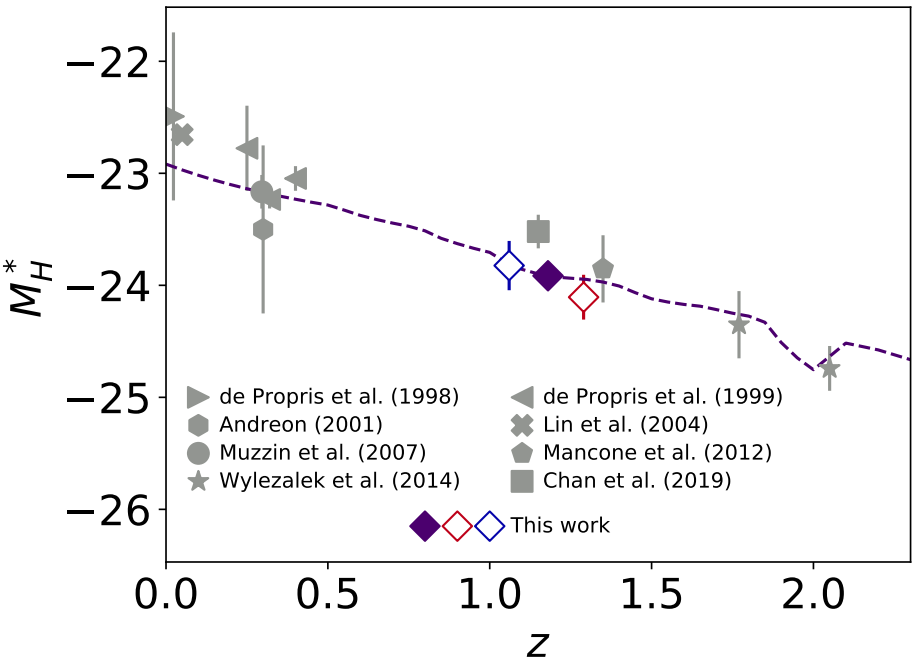

Figure 25 Absolute H-band characteristic magnitude versus redshift for a number of cluster LF studies. The error on the Lin et al. (2004) point is 0.02, smaller than the data marker. The dashed purple line shows the expected passive evolution in M^*_H, using the model described in §3.5.2.

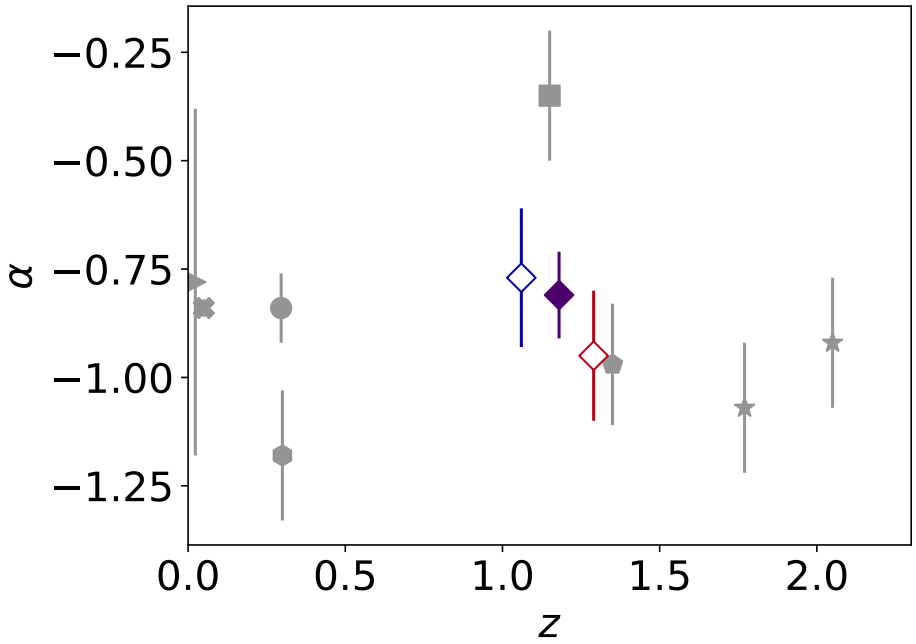

Figure 26 Faint-end slope versus redshift for a number of cluster LF studies. The labels for the points are the same as in Figure 25. The error on the Lin et al. (2004) point is 0.02, smaller than the data marker.

3.5.2.1 Comparisons at Similar Redshift

Owing to the difficulty in getting deep enough mid-infrared data, few studies have previously been able to measure both m^* and α simultaneously at this redshift range. One such study is Mancone et al. (2012), who measured composite LFs in 3.6 μm and 4.5 μm for seven IRAC Shallow Cluster Survey (ISCS) clusters at a median redshift of $z = 1.35$, slightly higher than our mean redshift overall, but a good match to our high-redshift sub-sample. Converting the apparent Vega magnitudes they report into absolute AB magnitudes, they found best fit parameters for the 3.6 μm LF of $M^*_H = -23.85 \pm 0.30$ and $\alpha = -0.97 \pm 0.14$. The faint-end slope we measure for the high-redshift clusters matches this result almost exactly and the characteristic magnitude we find is also consistent with their results.

Another similar study is Chan et al. (2019), who used IRAC 3.6 μm imaging to measure rest-frame H-band LFs for red-sequence galaxies in seven clusters from the infrared-selected Gemini Observations of Galaxies in Rich Early Environments (GOGREEN, Balogh et al., 2017) survey at a mean redshift of $\bar{z} = 1.15$. They report their results in terms of absolute H-band magnitudes and find $M^*_H = -23.52^{+0.15}_{-0.17}$, which is somewhat fainter than our value of $M^*_H = -23.91 \pm 0.12$ at $z = 1.18$. They also find a much more steeply falling faint-end slope than we do, with a value of $\alpha = -0.35 \pm 0.15$. This difference in α may be a result of their only including red-sequence galaxies, whereas we include everything with a photometric redshift consistent with being a cluster member. Other works (e.g., Muzzin et al., 2007; Strazzullo et al., 2006; De Propris, 2017) have found that the faint-end of the cluster

LF is dominated by blue galaxies, which would explain the discrepancy between our results and red-sequence-only results. Alternatively, Connor et al. (2019) found that the traditional model of the red sequence as a sloped line does not hold at fainter magnitudes. This could cause a drop-off in the measured red-sequence LF that is unconnected to the galaxy population of the cluster.

3.5.2.2 Comparisons at Other Redshifts

To put our results into a wider context, we also compare to studies at other redshifts and with different cluster selection and fitting methods. To make as fair a comparison as possible to m^* at other redshifts, we use the model described in §3.5.2 to convert all the magnitudes into the absolute H-band and limit ourselves to studies where the reported values still probe either the rest-frame H-band or nearby K-band. These comparisons are also shown in Figures 25 and 26.

At the lowest-redshift of our comparisons, de Propris et al. (1998) looked at the Coma cluster at $z = 0.023$ to a depth much fainter than m^*. They jointly fit m^* and α at magnitudes brighter than $m^* + 3$, though at magnitudes fainter than $m^* + 3$, they found a sharp rise in the number of galaxies and fit this with a power law. At a similar redshift, Lin et al. (2004) calculated a stacked K-band LF for a sample of 13 Abell clusters with X-ray follow-up. We compare to their joint fits of m^* and α, though they also attempt to fix α due to the uncertainty in the faint-end slope. Their errors on both parameters are 0.02, which is small enough it does not appear on Figures 25 and 26. At higher redshift, de Propris et al. (1999) looked at a

heterogenous selection of clusters in the K-band in redshift bins up to $z = 0.92$. They only fit to m^*, fixing the faint-end slope at $\alpha = -0.9$. We compare $z = 0.25$, $z = 0.32$ and $z = 0.4$ bins, where the conversion from K-band into rest-frame H-band has a minimal k-correction. Similarly, Muzzin et al. (2007), measured the observed-frame K-band for clusters at a mean redshift of $\bar{z} = 0.296$. In addition to reporting a composite LF for all galaxies in their clusters, Muzzin et al. (2007) also split their galaxies by whether they were quiescent or star-forming/recently-quenched. They found a relatively flat faint-end slope for their overall LF, $\alpha = -0.84 \pm 0.08$ and a much steeper faint-end slope of $\alpha = 0.17 \pm 0.18$ for red-sequence galaxies. At similar redshift, Andreon (2001) studied a single cluster at $z = 0.3$ in the K_S-band. He measured a LF down to $m^* + 5$ in various areas of the cluster, but the comparison we show is to the global values he reported. At higher redshifts, we also compare to some of the results from Wylezalek et al. (2014), who measured the 4.5 μm and 3.6 μm LF for clusters from the Clusters Around Radio Loud AGN program (CARLA, Wylezalek et al., 2013) in several redshift bins in the range $1.3 < z < 3.1$. We show two of these in Figures 25 and 26, again where the conversion from 3.6 μm or 4.5 μm has a minimal k-correction.

3.5.2.3 Evolution of the LF

Figure 25 shows the clusters in this work fall into a larger pattern of passive evolution in M_H^* going out to $z \sim 2$. Similarly, Figure 26 shows very little change in the faint-end slope over cosmic time when looking only at α over a range of studies. This

suggests that the evolution in the parameters shown in Figure 22 is primarily driven by passive evolution.

To confirm this, we evolution-correct the galaxies in the high- and low-redshift sub-samples to $z = 1.18$, the mean redshift of the full sample, assuming passive evolution. We then re-make the LFs and run the same joint fit as above. The results of this are shown in Figure 27. With passive-evolution 'baked-in' to the fit, the LF parameters are now consistent within two sigma, supporting the interpretation that these clusters are evolving passively, consistent with other studies at this redshift.

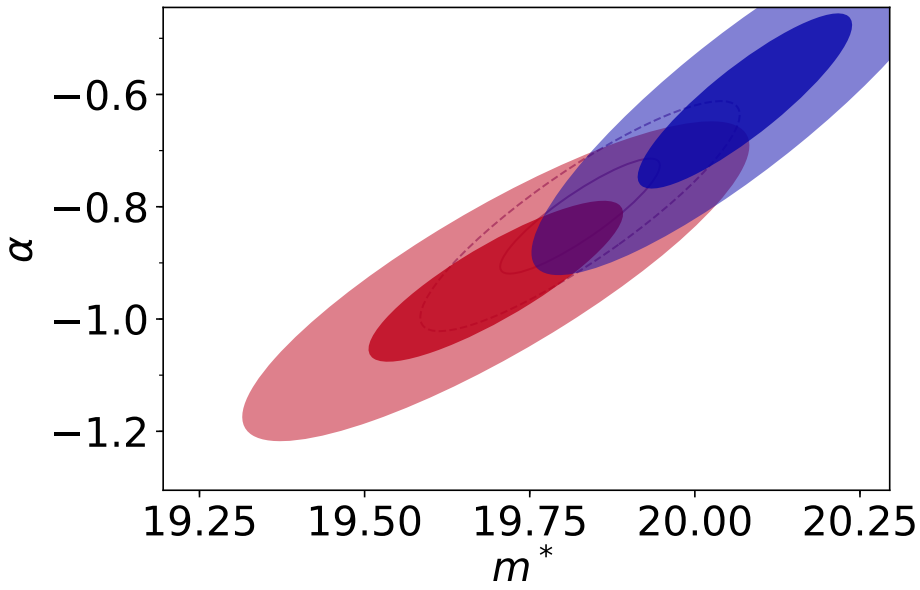

Figure 27 Covariance ellipses showing the 1σ (dark) and 2σ (light) errors and covariances in m^* and α for the high-redshift (red) and low-redshift (blue) sub-samples, *assuming passive evolution*. For comparison, the whole-sample covariances ellipses from Figure 20 are outlined underneath.

3.6 Conclusions

We have presented stellar mass fractions and 3.6 μm LFs for a sample of 12 infrared-selected clusters from the MaDCoWS catalog. We used optical and deep mid-IR follow-up data to fit SEDs to objects along the lines-of-sight to the clusters. This allowed us to more precisely identify cluster members, measure more thorough stellar masses for the clusters, and measure the faint-end slope of the LF.

The stellar mass fractions we report for these clusters are in good agreement with previous works, and are consistent with the Gonzalez et al. (2013) trend line with respect to total mass. For the individual clusters previously studied in Decker et al. (2019), the new values of $f_\star$ reported here are consistent with—but mostly higher than—the previous values, with much of the difference being attributable to the deeper data set we use here. By contrast, the stellar mass errors are now much smaller than in Decker et al. (2019), and the error on $f_\star$ is almost entirely driven by the uncertainty in the SZ mass measurements.

The composite 3.6 μm LF we fit for all 12 clusters has a best-fit characteristic magnitude and faint-end slope of $m^* = 19.83 \pm 0.12$ and $\alpha = -0.81 \pm 0.10$, respectively. Both are consistent with other works that have attempted to measure the rest-frame NIR LF for all cluster members at these redshift ranges. When we split our sample into a high-redshift bin at $\bar{z} = 1.29$ and a low-redshift bin at $\bar{z} = 1.06$ we find that there is a significant evolution in the best-fit Schechter function parameters, consistent with passive evolution. This significance is only seen in the covariance ellipse for m^* and α jointly. This highlights the need to study m^* and

α jointly. Comparing to works at other redshifts, our results are consistent with passive evolution since $z \sim 2$.

In future, follow-up data on more MaDCoWS clusters will allow us to better identify trends with redshift and other cluster parameters. In addition, deeper infrared data—such as will be attainable from the next generation of IR space telescopes—will allow us to more definitively answer questions about the evolution of the faint galaxy population in clusters at $z > 1$.

CHAPTER 4

CONCLUSIONS

In this thesis, I have focussed primarily on measuring the stellar mass-related properties of high-redshift infrared-selected galaxy clusters. I have measured the stellar mass fractions of these clusters in two different ways, as well as deep luminosity functions in the mid-infrared, where luminosity correlates strongly with stellar mass.

In Chapter 2, I used medium-deep *Spitzer*-IRAC photometry and a mass-to-light ratio from EZGal to measure the stellar mass fractions of infrared-selected MaDCoWS clusters and ICM-selected SPT clusters in the same range of mass and redshift. I used this to make a fair comparison of stellar mass fraction as a function of total cluster mass for both subsamples. I did not measure a significant difference between the samples, and what difference there was seemed to be driven by merging clusters. This suggests that the cluster selection method does not introduce a strong bias into the overall measurements of cluster composition, though the large scatter in the measured stellar mass fractions of the SPT clusters may be indicative of the IR-selected sample not being sensitive to the full range of stellar mass.

In Chapter 3, I made a more accurate measurement of the stellar mass fractions of a slightly different subset of MaDCoWS clusters. For this, I used very deep *Spitzer* observations, along with deep optical data to fit redshifts and stellar masses to objects along the lines-of-sight to the clusters and throw out the ones not lying

at the cluster redshift.

This improved method of measuring both membership and stellar mass of individual galaxies dramatically reduced the uncertainty in the measurement of the stellar mass of each cluster, minimizing this impact on the precision of the analysis. The limiting factor in this part of the analysis is the measurement of total cluster mass from the SZ effect. There is still enough scatter and uncertainty in the stellar mass *fraction* (which includes the now-dominant uncertainty of the total cluster mass) that it is hard to draw direct conclusions. Plotting stellar mass fraction versus total cluster mass, the clusters remain consistent both with the Gonzalez et al. (2013) line and with no correlation between total mass and stellar mass fraction. Future work will be able to combine other mass measurements—such as X-ray measurements from eROSITA, and improved SZ measurements from the next generation of surveys such as CMB-S—to reduce this uncertainty as well, and allow us to draw robust conclusions from this work.

Using these deep infrared data and improved membership determination I also measured luminosity functions, both for the full sample of clusters with the requisite data and for the high- and low-redshift subsets of these clusters. These LFs were complete more than two magnitudes fainter than m^*, allowing me to fit all parameters of the Schechter function simultaneously. Because of the strong covariance between α and m^*, this gives a much more robust measurement of each parameter than fitting them independently. The measured parameters showed significant evolution between the high- and low-redshift subsamples, but only when

viewing the joint fit to the parameters, further highlighting the necessity of getting sufficiently deep photometry to appropriately fit the faint-end slope along with the characteristic magnitude. The evolution itself is consistent with being caused by the passive evolution of the cluster galaxies between $z = 1.29$ and $z = 1.06$—after I applied a correction for this evolution, the evolution in the parameters was no longer significant.

Overall, I have shown that the MaDCoWS cluster sample is well-suited to measuring the evolution of cluster galaxies at a pivotal epoch in their development. Using the existing data on MaDCoWS clusters, I have shown there is no large-scale difference in cluster properties due to the selection method and I have highlighted the importance of using the uniquely deep photometry available for MaDCoWS clusters to measure cluster properties. These improved data will also help supply real comparisons to help guide the next generation of cosmic hydrodynamic simulations. As more and better follow-up data are taken on MaDCoWS clusters, we will be able to draw robust conclusions about the evolution of clusters at high-redshift.

APPENDIX A

A GUIDE TO THE CODE USED IN DECKER+22

The code used in the analysis presented in Chapter 3 and published in Decker et al. (2022) is available at `https://github.com/bandondecker/legacy_code_for_decker_22`. This appendix is a guide to the use of that code to replicate the analysis.

The analysis is done by a suite of scripts, run in roughly the order they are listed below. Altogether, they SWarp the cluster images onto a common scale (that of the Gemini images), put those images into a single directory, make four-band catalogues for each cluster, run SED-fitting code on all of the catalogues, assign membership probability, create 'members-only' catalogues, calculate the stellar mass and stellar mass fraction, write that to a table, make the plots for $f_\star$, calculate the LFs, fit the Schechter function to the LFs, write all the results out to files, and finally make the LF and fitting plots.

The code is modular, so a lot of the features can be turned on or off, and scripts 'downstream' generally only need output files written from the earlier scripts, reducing how many need to be re-run.

A.1 `swarpImsMakeCats.py`

This is the script to SWarp the images onto a common scale and make the four-band catalogues. It takes as dependencies several `astropy` modules, though only `ascii`,

`fits`, and `table` are still needed. It also takes two other modules I wrote. One is `sextractor` and is a wrapper for SE. The other is the `tools` module described above, but it no longer serves any purpose in this code.

Originally this code also removed from the catalogues objects outside of r_{500} and with an SNR less than five in the detection band. These were later moved to `membershipID.py`, but there are still relic lines related to this, including some of the imported modules.

Like all of the scripts in this section, it is designed to be run from the command line with:

```
$ python swarpImsMakeCats.py
```

Unlike a lot of the later-written scripts though, the modularity of this script is not controlled with flags. Instead the user is expected to comment or uncomment lines in the script section as-needed.

The script section begins at line 239 and reads in the table of clusters and cluster properties, and the table of sky errors. Note that both of these are hard-coded to the directory structure in which the code was written. The rest is a loop over the clusters that sets cluster properties and calls the functions defined earlier in the code.

The `idFiles()` function sets the image filenames to use. The original images, and the SWarped images are returned as lists. It also returns the detection image, but this is relic code that now only serves to identify the location of the IRAC images. All of the image locations are hard-coded.

The `doSwarp()` function is likely to only be needed once. It takes the lists of original and target images from `idFiles()` and runs SWarp to make the new images. Once this is done satisfactorily it never needs to be done again. **NB: This does not render the original images redundant.** The way SWarp is called in this doesn't transfer most of the header data to the new images and the zero point of the Gemini images is defined in the header of the originals.

The `makeMainCat()` function runs SE in dual-image mode on the cluster images to make a basic four-band catalogue. It writes this to disc, but it also returns the AstroPy `Table` object to save processing time in the next steps. This is now hard-coded to use the SWarped IRAC 3.6 μm image as the detection image, though there was previously an option to set the detection image, and there is still some relic code referencing that.

The base catalogue is processed with `processCat()`. This is the most pared-down function in the file, as previously this did an SNR cut and a cut on distance from the cluster centre. Now its only function is to set an error floor for each object of 3% and write out a new catalogue. (Note that it does not overwrite the original, this is a relic from when the changes were more substantial.) It can take in a catalogue as an AstroPy Table, but if not given one it will read in the catalogue using the cluster name and assuming the nomenclature used by `makeMainCat()`.

The last function, and the one that most frequently needs to be updated, is `fitCat()`. This function takes the processed catalogue and re-writes it into a format used by the SED-fitting software. As that changes, this function needs to be

re-written. It writes the output catalogues directly into the directories used by the fitting codes, instead of the directory used for the rest of this analysis.

A.2 `runEazyFast.py`

This is the script to run the SED-fitting codes EAZY (for the redshifts) and FAST (for the stellar masses). The process it runs is slightly convoluted to account for the idiosyncrasies of the software it is calling. There are no non-standard dependencies.

This code runs EAZY on the background catalogue (this is assumed to have been created already, and the location is hard-coded) and then loops through the clusters. In theory, EAZY parameters can be adjusted when it is called from the command line. However, this has never worked the way it is described by the authors. For each cluster, this script opens the EAZY parameter file, and changes the inputs there, then runs EAZY.

For simplicity, the code also changes the FAST parameter file for each cluster and the background. Each time it sets the redshift of every object to the cluster redshift, and calculates the stellar mass based on that assumption. (Objects for which that is not a fair assumption are thrown out later anyway, but this means the fitting does not need to be re-run if we change the membership probability threshold.)

After running this code, there will be output files from EAZY and FAST all written to directories *in the main analysis directory.*

A.3 membershipID.py

This code calculates the membership probability of all objects in the cluster and background catalogues and writes out 'members-only' catalogues and stellar mass output files. The script is called from the command lines with the optional flags `-r` and `-p`

```
$ python membershipID.py -r -p
```

NB: These have to be called as separate flags, calling `-rp` won't register either one. (This could be fixed.)

The `-r` flag is 'recalc'. This will tell the code to calculate or re-calculate the membership probability for all the objects. This section of the code reads in the redshift PDFs from EAZY and convolves them with a Gaussian of the width of the scatter in the best-fit redshifts. This scatter is calculated with a small separate code that compares the best-fit redshifts of the background to those of COSMOS, called `iterative_sig_clip_scatter.py`. It's not required to run this code; the error calculated from it is hard-coded in line 60 of `membershipID.py`.

The script uses a trapezoidal integration function defined in the file to calculate the integrated probability under the convolved PDF in the range of the cluster redshift. It write this probability as a new column to the cluster catalogue, the background catalogue, the cluster stellar mass output file, and the background stellar mass output file. This is a slow-ish calculation, so a handful of print statements are included to give a sense of progress. Because it's fairly slow, it's not recommended to recalculate the probabilities unless it's needed.

if the `-p` flag is enabled, the script will also plot the convolved redshift PDF and the integration range around the cluster redshift *for each object*. This is obviously a *very* slow process and one that uses up a lot of memory. It's very good for sanity checking and produces one of the plots in Decker et al. (2022), but it is not recommended to run it often. It also relies on 'recalc' being called—the plotting loop is inside the recalc loop—so calling `-p` without `-r` will not have any effect.

Regardless of the flags, the code will always read in the background and cluster catalogues and stellar mass output files. Assuming 'recalc' has been called at some point, these will include 'intprob' columns with the integrated probability. There is a probability threshold defined in line 59 of the code, but after we settled on 0.3 as an unchangeable threshold, this was hard-coded instead. The script will cut anything below that threshold, anything outside of r_{500} from the cluster centre and anything with an SNR in 3.6 μm below five in both the catalogues and stellar mass files.

The code will write out four files for each cluster, two in the catalogues directory and two in the stellar mass directory. In the catalogues directory it will write the 'members-only' cluster catalogue and a corresponding catalogue for the background assuming the cluster redshift, and in the stellar mass directory it will write catalogues of the same objects, but with the FAST outputs. These are all labelled 'intprob'; this is a relic of experimentation of different possible cuts to isolate cluster members. (This is relevant for some downstream scripts.)

A.4 `calcFStars.py`

This is the code to calculate the stellar mass and $f_\star$ for each cluster, write those to a table, and make the $f_\star$ plots. The calculation of the stellar mass is fairly quick, but for the sake of efficiency it is an optional routine, called with the flag `-recalc`.

```
$ python calcFStars.py -recalc
```

(A possible improvement for the future would be to make the flags consistent between this and `membershipID.py`.) There is also some relic code regarding an option to use the membership completeness correction. This is now set to `True` regardless of input, but the completeness routine is still in an `if` statement.

For each cluster, the stellar mass calculation reads in the four files written for that cluster by `membershipID.py`, scales the stellar mass by the completeness of the object (photometric and membership) and sums them together. It scales the background to the cluster area and subtracts that from the cluster mass. It also calculates the error at the same time.

For each cluster, the stellar mass, stellar mass error, $f_\star$ and $f_\star$ error are all added to the cluster properties table and written as a new table `clusters_w_output.py`.

Regardless of if the stellar masses are recalculated, the code also reads in the output table and also the output table from the Decker et al. (2019) analysis to make the main $f_\star$ versus total mass plot and the plot of new $f_\star$ versus old $f_\star$.

A.5 `fitLF.py`

This is the script to make the composite LFs, fit Schechter functions to them, and write both the LFs and the fit parameters to files. This function has gone through several revisions over the course of the project and has the most idiosyncrasies and relic code. This code calls `MCMC_LF.py` to do the LF fitting. That code is described in §A.7.

Most of the work in this script is done by the function `makeLF()`, which takes as input the catalogue of clusters that are being stacked and the magnitude bins of the LF. It reads in the catalogues of each cluster in the input table and the background for that cluster, as well as the completeness functions to make an appropriately weighted LF and LF errors. It also outputs the full line-of-sight LF and the background LF that is subtracted off, for sanity checking.

There are also relic inputs for the probability threshold, leftover from when I wanted to compare the effect of different thresholds. This is set to 0.3 as a default, and should be removed as an option altogether. There is also a keyword for the 'title' of the analysis. This dates back to when there were different catalogues with different membership determinations. This is now set to 'comp' as the default, which will read in the 'intprob' catalogues and apply the completeness corrections. This should also be removed as an option.

A lot of the detail in the `makeLF()` function revolves around correctly calculating the uncertainty in each bin and trying to keep a good 'running tally' of everything. However there are a couple of other small details, one of which needs

to be fixed. When the LFs are scaled to being per magnitude and per cluster, it assumes that each histogram bin is a quarter of a magnitude wide and multiplying by 4.0 is hard coded. This will give bad results if other bin widths are entered, and this should be fixed.

The code outside the `makeLF()` function sets the magnitude bins to be used for each LF, and sets the loop to do multiple subsamples. The number of subsamples are set by the user when the function is called. There is also an option to make subsets with the faint end not fit. These are related; the first two subsets are the high- and low-redshift LFs. Subsequent subsets, up to five, are the same set of overall LF, high-redshift LF and low-redshift LF, but with the faint-end cutoff. The code will automatically cap the number of subsets at five.

Calling the function from the command line, the first argument is to be the (now redundant) title of the analysis. This should always now be 'comp'. The second is the number of subsets to make LFs. Note that the number of subsets does *not* include the overall LF. So setting this to '2' will produce the overall LF, and high- and low-redshift LFs. The last input number is how many bins to omit when not fitting to the faint end. This is called as a negative number, as it is directly used as the index on which to slice the LFs. So setting it to '-1' will drop the last bin. This will only be relevant if the number of subsets is at least three, as it is only subsets after the first two that will take the cutoff. If neither the number of subsets or the faint-end cutoff are specified, they will default to '0' and '-1', respectively. The full call then looks something like the following:

```
$ python fitLF.py comp 0 -1
```

For the final analysis as published, there is now no more need for any of these items. They could all be hard-coded.

The LF for each subset will be written to a table with columns of magnitude bins, the composite LF, the full line-of-sight LF and the background LF, and errors for all.

The code takes the LF and LF error from `makeLF()` and calls `MCMC_LF.MCMC()` to fit the Schechter function. The arguments are all hard coded; there are flat priors around all the Schechter parameters, ten walkers taking 110000 steps with a burn-in period of 10000 steps. These can be changed in the code itself, but should be consistent for all the fits. With these parameters, the fit only takes a few minutes per subset. `MCMC()` returns the full chains as AstroPy tables and `fitLF.py` pickles these and saves them to the chains directory. (Pickling has proved to be the most straightforward way to preserve the chains, rather than simply write a text file, but this could be addressed in the future.) These are used for the plots later.

The best-fit values and errors are calculated as the mean and standard deviation of the walker values. These are printed to the screen and saved to a table of Schechter function parameters. The posterior likelihoods are also saved, though in the current analysis (without the double-Schechter function comparison) this isn't used.

There are also closely-related functions in the repository dealing with fitting to absolute magnitudes and evolution-corrected LFs. These are for the most part

identical, and ideally should be made into optional functionality of the main code.

A.6 `makePlots.py`

This is the code to make all of the plots related to the LFs and fitting. It used to be called with the same options as `fitLF.py` (in fact it started as part of the same script), but the options that should be removed and hard-coded from `fitLF.py` largely *have* been removed from `makePlots.py`. The only option callable from the command line now is `-abs` which will plot everything in absolute magnitudes instead of apparent mags. This isn't used, however.

The code has two parts. The first part loops through the three LFs—the overall LF, and the high- and low-redshift LFs—and reads in the LFs, the Schechter function parameters and loads in the chains. It makes four plots for each LF: A simple LF-only plot, a plot with both the LF points and the fit Schechter function, along with annotations giving the parameters, the same plot but with a shaded fit showing the error on the parameters (this and the previous plot are very useful for meeting slides), and finally the paper-style plots in a better aspect ratio without the annotations. It also makes the α versus m^* covariance ellipse for each fit.

All of the plots with the shaded error region are very resource-intensive to make. They read in the full chains from `MCMC_LF.MCMC()` and use the 68% interval, to define the shaded region, but the chains are so long it uses a lot of memory and processing power to find the appropriate region. These regions can be commented out to make some of the other plots run faster.

There is also relic code in this area dealing with the subsets that do not fit the very faintest end, but the loop is hard-coded not to include these now.

The second part makes the plots that directly compare different LFs and different fits. The first is the two-panel plot of the high- and low-redshift LFs with the shaded fit regions. The second plot is the overlapping covariance ellipses for the same subsets, with the outline of the main LF ellipse.

A.7 `MCMC_LF.py`

This is a module of functions relating to the MCMC fitting for the Schechter function. The functions themselves are described in the docstrings, but it is important to note that this is limited to fitting a Schechter function or a double-Schechter function to a luminosity function created by `fitLF.py`. There are options for setting flat priors or Gaussian priors. The main function to call `MCMC_LF.MCMC()` returns the fitting chains, and most of the other functions in the module are support functions for that.

There is also a more general `MCMC.py` module in development, which is an extension of this module designed to be more generally applicable, and to have the code to make output diagnostic plots built in. This is still very much a work-in-progress though, and is not ready to be used as-is.

REFERENCE LIST

Allen, S. W., Evrard, A. E., & Mantz, A. B. 2011, ARA&A, 49, 409

Andersson, K., Benson, B. A., Ade, P. A. R., et al. 2011, ApJ, 738, 48

Andreon, S. 2001, ApJ, 547, 623

Andreon, S. 2010, MNRAS, 407, 263

Arnaud, M., Pratt, G. W., Piffaretti, R., et al. 2010, A&A, 517, A92

Ashby, M. L. N., Stern, D., Brodwin, M., et al. 2009, ApJ, 701, 428

Ashby, M. L. N., Willner, S. P., Fazio, G. G., et al. 2013, ApJ, 769, 80

Balogh, M. L., Gilbank, D. G., Muzzin, A., et al. 2017, MNRAS, 470, 4168

Bertin, E. & Arnouts, S. 1996, A&AS, 117, 393

Bertin, E., Mellier, Y., Radovich, M., et al. 2002, in Astronomical Society of the Pacific Conference Series, Vol. 281, Astronomical Data Analysis Software and Systems XI, ed. D. A. Bohlender, D. Durand, & T. H. Handley, 228

Bleem, L. E., Stalder, B., de Haan, T., et al. 2015, ApJS, 216, 27

Brammer, G. B., van Dokkum, P. G., & Coppi, P. 2008, ApJ, 686, 1503

Brodwin, M., Stanford, S. A., Gonzalez, A. H., et al. 2013, ApJ, 779, 138

Brodwin, M., Greer, C. H., Leitch, E. M., et al. 2015, ApJ, 806, 26

Bruzual, G. & Charlot, S. 2003, MNRAS, 344, 1000

Chabrier, G. 2003, PASP, 115, 763

Chambers, K. C., Magnier, E. A., Metcalfe, N., et al. 2016, ArXiv e-prints, arXiv:1612.05560 [astro-ph.IM]

Chan, J. C. C., Wilson, G., Rudnick, G., et al. 2019, ApJ, 880, 119

Chiu, I., Mohr, J., McDonald, M., et al. 2016, MNRAS, 455, 258

Chiu, I., Mohr, J. J., McDonald, M., et al. 2018, MNRAS, 478, 3072

Connor, T., Kelson, D. D., Donahue, M., & Moustakas, J. 2019, ApJ, 875, 16

Conroy, C., Wechsler, R. H., & Kravtsov, A. V. 2007, ApJ, 668, 826

Cutri, R. M. 2013, VizieR Online Data Catalog, 2328, 0

Davis, M., Guhathakurta, P., Konidaris, N. P., et al. 2007, ApJL, 660, L1

de Haan, T., Benson, B. A., Bleem, L. E., et al. 2016, ApJ, 832, 95

De Propris, R. 2017, MNRAS, 465, 4035

de Propris, R., Eisenhardt, P. R., Stanford, S. A., & Dickinson, M. 1998, ApJL, 503, L45

de Propris, R., Stanford, S. A., Eisenhardt, P. R., Dickinson, M., & Elston, R. 1999, AJ, 118, 719

Decker, B., Brodwin, M., Abdulla, Z., et al. 2019, ApJ, 878, 72

Decker, B., Brodwin, M., Saha, R., et al. 2022, arXiv e-prints, arXiv:2112.12239

Di Mascolo, L., Mroczkowski, T., Churazov, E., et al. 2020, A&A, 638, A70

Dicker, S. R., Romero, C. E., Di Mascolo, L., et al. 2020, ApJ, 902, 144

Eisenhardt, P. R., Stern, D., Brodwin, M., et al. 2004, ApJS, 154, 48

Ettori, S., Dolag, K., Borgani, S., & Murante, G. 2006, MNRAS, 365, 1021

Fazio, G. G., Hora, J. L., Allen, L. E., et al. 2004, ApJS, 154, 10

Gaia Collaboration, Prusti, T., de Bruijne, J. H. J., et al. 2016, A&A, 595, A1

Gaia Collaboration, Brown, A. G. A., Vallenari, A., et al. 2018, A&A, 616, A1

Gettings, D. P., Gonzalez, A. H., Stanford, S. A., et al. 2012, ApJL, 759, L23

Giodini, S., Pierini, D., Finoguenov, A., et al. 2009, ApJ, 703, 982

Gonzalez, A. H., Sivanandam, S., Zabludoff, A. I., & Zaritsky, D. 2013, ApJ, 778, 14

Gonzalez, A. H., Zaritsky, D., & Zabludoff, A. I. 2007, ApJ, 666, 147

Gonzalez, A. H., Decker, B., Brodwin, M., et al. 2015, ApJL, 812, L40

Gonzalez, A. H., Gettings, D. P., Brodwin, M., et al. 2019, ApJS, 240, 33

Hainline, L. J., Blain, A. W., Smail, I., et al. 2011, ApJ, 740, 96

He, P., Feng, L.-L., & Fang, L.-Z. 2005, ApJ, 623, 601

Hilton, M., Hasselfield, M., Sifón, C., et al. 2013, MNRAS, 435, 3469

Högbom, J. A. 1974, A&AS, 15, 417

Hook, I. M., Jørgensen, I., Allington-Smith, J. R., et al. 2004, PASP, 116, 425

Jannuzi, B. T. & Dey, A. 1999, in Astronomical Society of the Pacific Conference Series, Vol. 191, Photometric Redshifts and the Detection of High Redshift Galaxies, ed. R. Weymann, L. Storrie-Lombardi, M. Sawicki, & R. Brunner, 111

Kauffmann, G. & Charlot, S. 1998, MNRAS, 297, L23

Krause, E., Pierpaoli, E., Dolag, K., & Borgani, S. 2012, MNRAS, 419, 1766

Kravtsov, A. V. & Borgani, S. 2012, ARA&A, 50, 353

Kravtsov, A. V., Nagai, D., & Vikhlinin, A. A. 2005, ApJ, 625, 588

Kriek, M., van Dokkum, P. G., Labbé, I., et al. 2009, ApJ, 700, 221

Lacy, M., Wilson, G., Masci, F., et al. 2005, ApJS, 161, 41

Laigle, C., McCracken, H. J., Ilbert, O., et al. 2016, ApJS, 224, 24

Lan, T.-W., Ménard, B., & Mo, H. 2016, MNRAS, 459, 3998

Lin, Y.-T., Mohr, J. J., & Stanford, S. A. 2003, ApJ, 591, 749

Lin, Y.-T., Mohr, J. J., & Stanford, S. A. 2004, ApJ, 610, 745

Lin, Y.-T., Stanford, S. A., Eisenhardt, P. R. M., et al. 2012, ApJL, 745, L3

Mancone, C. L. & Gonzalez, A. H. 2012, PASP, 124, 606

Mancone, C. L., Gonzalez, A. H., Brodwin, M., et al. 2010, ApJ, 720, 284

Mancone, C. L., Gonzalez, A. H., Brodwin, M., et al. 2012, ApJ, 761, 141

Marrone, D. P., Smith, G. P., Okabe, N., et al. 2012, ApJ, 754, 119

McCarthy, I. G., Schaye, J., Bird, S., & Le Brun, A. M. C. 2017, MNRAS, 465, 2936

McLean, I. S. et al. 2010, in Proc. SPIE, Vol. 7735, Ground-based and Airborne Instrumentation for Astronomy III, 77351E

McLean, I. S. et al. 2012, in Proc. SPIE, Vol. 8446, Ground-based and Airborne Instrumentation for Astronomy IV, 84460J

Mo, W., Gonzalez, A., Stern, D., et al. 2018, ApJ, 869, 131

Muzzin, A., Wilson, G., Lacy, M., Yee, H. K. C., & Stanford, S. A. 2008, ApJ, 686, 966

Muzzin, A., Yee, H. K. C., Hall, P. B., Ellingson, E., & Lin, H. 2007, ApJ, 659, 1106

Nurgaliev, D., McDonald, M., Benson, B. A., et al. 2017, ApJ, 841, 5

Oke, J. B., Cohen, J. G., Carr, M., et al. 1995, PASP, 107, 375

Orlowski-Scherer, J., Di Mascolo, L., Bhandarkar, T., et al. 2021, A&A, 653, A135

Pillepich, A., Nelson, D., Hernquist, L., et al. 2017, ArXiv e-prints, arXiv:1707.03406

Planelles, S., Borgani, S., Dolag, K., et al. 2013, MNRAS, 431, 1487

Poole, G. B., Babul, A., McCarthy, I. G., et al. 2007, MNRAS, 380, 437

Rudy, D. J., Muhleman, D. O., Berge, G. L., Jakosky, B. M., & Christensen, P. R. 1987, Icarus, 71, 159

Salpeter, E. E. 1955, ApJ, 121, 161

Schechter, P. 1976, ApJ, 203, 297

Scoville, N., Aussel, H., Brusa, M., et al. 2007, ApJS, 172, 1

Stanford, S. A., Gonzalez, A. H., Brodwin, M., et al. 2014, ApJS, 213, 25

Strazzullo, V., Rosati, P., Stanford, S. A., et al. 2006, A&A, 450, 909

Sunyaev, R. A. & Zeldovich, I. B. 1980, ARA&A, 18, 537

Sunyaev, R. A. & Zeldovich, Y. B. 1970, Comments on Astrophysics and Space Physics, 2, 66

Sunyaev, R. A. & Zeldovich, Y. B. 1972, Comments on Astrophysics and Space Physics, 4, 173

van der Burg, R. F. J., Muzzin, A., Hoekstra, H., et al. 2014, A&A, 561, A79

White, S. D. M., Navarro, J. F., Evrard, A. E., & Frenk, C. S. 1993, Nature, 366, 429

Wright, E. L., Eisenhardt, P. R. M., Mainzer, A. K., et al. 2010, AJ, 140, 1868

Wylezalek, D., Galametz, A., Stern, D., et al. 2013, ApJ, 769, 79

Wylezalek, D., Vernet, J., De Breuck, C., et al. 2014, ApJ, 786, 17

Zhang, Y.-Y., Laganá, T. F., Pierini, D., et al. 2011, A&A, 535, A78

VITA

Bandon Decker was born on 12th November, 1988 in Kansas City, Missouri. In 2007 he graduated with an Associate of Arts degree from Maple Woods Community College in Kansas City and in 2009 he graduated *cum laude* from Truman State University with a Bachelor of Science degree in physics. He has been a graduate student at UMKC since the autumn of 2013.